

Article

# Plasma-Catalytic Fischer–Tropsch Synthesis at Very High Pressure

Byron Bradley Govender, Samuel Ayodele Iwarere \*  and Deresh Ramjugernath

Thermodynamics Research Unit, Howard College Campus, School of Engineering, College of Agriculture, Engineering and Science, University of KwaZulu-Natal, Durban 4041, South Africa; byron.bg1@gmail.com (B.B.G.); ramjuger@ukzn.ac.za (D.R.)

\* Correspondence: iwarere@ukzn.ac.za

**Abstract:** This study explored Fischer–Tropsch synthesis (FTS) by combining a non-thermal plasma (NTP), generated by an arc discharge reactor at pressures  $\gg 1$  MPa, coupled with a mullite-coated 2 wt%–Co/5 wt%–Al<sub>2</sub>O<sub>3</sub> catalyst. The FTS product yields and electrical energy consumption for the pure plasma (no catalyst) and plasma-catalytic FTS processes were compared under the scope of various reactor operating parameters, namely, pressure (0.5 to 10 MPa), current (250 to 450 mA) and inter-electrode gap (0.5 to 2 mm). The major products, obtained in low concentrations for both processes, were gaseous C<sub>1</sub>–C<sub>3</sub> hydrocarbons, synthesised in the order: methane  $\gg$  ethane > ethylene > propane. The hydrocarbon product yields were observed to increase, while the specific required energy generally decreased with increasing pressure, decreasing current and increasing inter-electrode gap. Plasma-catalysis improved the FTS performance, with the optimum conditions as: (i) 10 MPa at 10 s and 2 MPa at 60 s for the pressure variation study with the longer treatment time producing higher yields; (ii) 250 mA for the current variation study; (iii) 2 mm for the inter-electrode gap variation study. Plasma-catalysis at a gap of 2 mm yielded the highest concentrations of methane (15,202 ppm), ethane (352 ppm), ethylene (121 ppm) and propane (20 ppm), thereby indicating the inter-electrode gap as the most influential parameter.

**Keywords:** non-thermal plasma; high pressure; arc discharge; Fischer–Tropsch synthesis; cobalt catalyst



**Citation:** Govender, B.B.; Iwarere, S.A.; Ramjugernath, D.

Plasma-Catalytic Fischer–Tropsch Synthesis at Very High Pressure. *Catalysts* **2021**, *11*, 297. <https://doi.org/10.3390/catal11030297>

Received: 17 December 2020

Accepted: 12 January 2021

Published: 25 February 2021

**Publisher's Note:** MDPI stays neutral with regard to jurisdictional claims in published maps and institutional affiliations.



**Copyright:** © 2021 by the authors. Licensee MDPI, Basel, Switzerland. This article is an open access article distributed under the terms and conditions of the Creative Commons Attribution (CC BY) license (<https://creativecommons.org/licenses/by/4.0/>).

## 1. Introduction

Fischer–Tropsch synthesis (FTS), a process used to produce synthetic fuels (synfuels) from syngas (CO and H<sub>2</sub>), has been a competitive alternative to oil-derived fuels for almost a century and is positioned to play a more significant role in the global energy mix in upcoming decades due to diminishing oil reserves and rising energy demand [1]. This trend is suggested by continuous investments in FTS infrastructure and feedstock exploration by the world's major energy providers [2,3]. Besides FTS being used to produce synfuels to power automobiles, the process has recently been explored for the production of synthetic jet fuels as alternative fuels in commercial [4] and military aviation [5,6]. In addition, the National Aeronautics and Space Administration (NASA) has been investigating the FTS middle distillate (C<sub>8</sub>–C<sub>18</sub> hydrocarbons) for aerospace applications [7,8].

Due to the widespread interest in FTS, much research has been focused on improving FTS' performance by formulating proprietary catalysts [9] and developing reactor technologies [10]. Most FTS studies maintain the conventional operation conditions, namely, pressures between 2 and 4 MPa, temperatures between 220 and 240 °C and reaction periods of hours to weeks with either a cobalt or iron-based catalyst [11–13].

A recent alternative to conventional FTS methods has been non-thermal plasma technologies (NTPs). These may become competitive with conventional FTS due to the short reaction times, room temperature operation (no external heating required) and reduced equipment space requirements. However, despite the benefits of NTPs, NTP-induced FTS has scarcely been studied with a few known studies at atmospheric pressure [14] and very high pressure [15,16].

In FTS, using very high-pressure NTPs [15,16], C<sub>1</sub>–C<sub>3</sub> hydrocarbons were produced from syngas (CO + H<sub>2</sub>) in an arc discharge reactor at reaction times of seconds to slightly over a minute, without external heating of the reactor and without a catalyst present [15,16]. Incorporating an FTS catalyst in a high-pressure arc discharge reactor—a process known as plasma-catalysis—should increase the hydrocarbon yields and product distribution due to the interactions between the active NTP species and catalyst, results which were observed in other plasma-catalytic applications. The introduction of a catalyst into an atmospheric pressure NTP has been shown to enhance the energy efficiency through different enhancement mechanisms [17], extend the plasma region in microdischarges through propagation along the solid surface [17] and increase the concentration and residence time of plasma species in discharge zone [18,19]. The NTP, in turn, may reduce the catalyst's activation temperature (increasing the catalyst's lifetime [20,21]) and thermally activate (heat) the catalyst [22–27], enhance chemisorption on the catalyst surface [28] and reduce and/or disperse the catalytic material [29–31].

These plasma–catalyst interactions at sub-atmospheric to atmospheric pressures were considered to be responsible for increasing the product yields and energy efficiency compared to the sum of the individual pure plasma (no catalyst) and pure catalysis (no plasma) processes, which were observed in widely researched applications such as volatile organic compounds (VOCs) treatment [32,33] and dry reforming of methane [21,34,35]. In some dry reforming cases, plasma-catalysis led to doubling of the hydrogen product yields compared to the pure plasma process [34–36].

Chu et al. [37] reported on the performance of cobalt catalysts pretreated with glow-discharge plasma in Fischer–Tropsch synthesis at 1 bar and low temperature. The authors reported that the pretreatment of the catalyst improved carbon monoxide (CO) conversion and methane selectivity. However, for longer-chain hydrocarbons (C<sub>5+</sub>), similarities were seen between its selectivity and those prepared through conventional techniques.

More current advancement in hydrocarbon synthesis through FTS has employed the application of induction suspension plasma technology [38], with reported preparation of nanometric C-supported catalysts [39]. These plasma-synthesized catalysts have been shown to have active catalytic species for FTS using Co-based and modified Co–Fe catalysts [40,41]. Aluha et al. [42] provided a short review paper highlighting advances made from the introduction of plasma techniques for catalyst synthesis since its introduction four decades ago. The authors further reported experimental results from a PL-50 plasma torch generated with radio frequency alternating currents, showing an improved selectivity towards the longer-chain hydrocarbons for Co/C catalyst at 493 K, 2 MPa and 3600 cm<sup>3</sup>·h<sup>−1</sup>·g<sup>−1</sup> gas hourly space velocity.

However, only a few experimental results are available in literature on plasma-catalysis with non-thermal discharges applied in FTS, where methane formation was suppressed and chain growth was improved compared to pure catalytic FTS at pressures between 0.1 and 0.6 MPa [14,43,44].

Based on these benefits, arising from the plasma–catalyst synergy in atmospheric pressure processes, including in FTS applications, this study investigated very high-pressure plasma-catalysis at pressures between 1 and 10 MPa. This was accomplished by incorporating an industrially representative cobalt FTS catalyst into a very high-pressure arc discharge reactor. Unlike most atmospheric pressure NTP reactors, such as the dielectric barrier discharge, where the catalyst is directly inserted between the electrodes (in-plasma catalysis (IPC)) [14], the high-temperature arc core (T > 10,000 K) and minimal space (volume ~2.56 cm<sup>3</sup>), in the very high-pressure arc discharge reactor, prevents an IPC arrangement of the catalyst.

Therefore, the novelty of the study presented here, lies in its exploration of the pressure range, which has not been studied in the framework of plasma-catalysis for chemical synthesis, along with a catalyst configuration within the arc discharge reactor, which has not been previously reported.

First, an industrially representative 2 wt%-Co/Al<sub>2</sub>O<sub>3</sub> FTS catalyst was prepared and coated onto a mullite substrate, and thereafter the performance of the plasma-catalytic FTS was determined in comparison with the pure plasma FTS, which was separately carried out. These two process performances were based on the influence of three operating parameters on the hydrocarbon yields and energy consumption. The operating parameters were pressure (i.e., 0.5 to 10 MPa), current (i.e., 200 to 450 mA) and inter-electrode gap (i.e., 0.5 to 2 mm).

## 2. Results

The concentration of the C<sub>1</sub>–C<sub>3</sub> gaseous hydrocarbons, produced in the arc discharge reactor for both the pure plasma and plasma-catalytic systems, were determined using Equations (1)–(3). Low concentrations of the C<sub>1</sub> to C<sub>3</sub> hydrocarbons were produced as the arc discharge active volume—the volume consisting of active plasma species responsible for promoting FTS reactions—was approximately 10<sup>5</sup> lower than the total volume of the arc discharge reactor (2.56 cm<sup>3</sup>), resulting in dilution of the FTS products with unreacted syngas.

The three parameters that were investigated and reported in this paper are the operating pressure, the supplying current and the inter-electrode gap. The results of the influence of these parameters on the pure plasma and plasma-catalytic FTS are presented and discussed through Sections 2.1–2.3.

### 2.1. The Influence of Pressure on Plasma-Catalytic FTS

In order to study the effect of very high pressures on the gaseous hydrocarbon yields and energy consumption for pure plasma and plasma-catalytic FTS, the supplying current and inter-electrode gap were fixed at 350 mA and 1 mm, respectively, at different discharge times of 10 and 60 s. The operating conditions are listed in Table 1.

The methane, ethane, ethylene and propane concentrations versus pressure curves for pure plasma and plasma-catalytic FTS, at the above-mentioned operating conditions, are presented in Figure 1a–d.

**Table 1.** List of operating conditions used in pure plasma and plasma-catalytic Fischer–Tropsch synthesis (FTS).

Operating Parameters	Pressure Variation Study		Current Variation Study	Electrode Gap Variation Study
Discharge time (s)	10	60	60	60
Operating current (mA)	350	350	250, 300, 350, 400, 450	350
Ignition voltage (kV)	8	8	8	8
Inter-electrode gap (mm)	1	1	1	0.5, 1.0, 1.5, 2.0
Pressure (MPa)	0.5, 1, 2, 3, 4, 5, 6, 7, 8, 9, 10	0.5, 1, 2, 3, 4, 5, 6, 7, 8, 9, 10	2	2
H <sub>2</sub> /CO ratio	2.2:1	2.2:1	2.2:1	2.2:1

#### 2.1.1. Pure Plasma

For pure plasma FTS, the methane concentration curves at 10 and 60 s (shown in Figure 1a) increased monotonically with increasing pressure from 1 to 10 MPa. In the 60 s study, the methane concentration was at a minimum of 32 ppm at 1 MPa and a maximum of 772 ppm at 10 MPa. In the 10 s study, the methane concentration was at a minimum of 17 ppm at 1 MPa and a maximum of 342 ppm at 10 MPa. Both the 10 and 60 s studies produced similar methane concentrations between 1 and 4 MPa. However, from 6 MPa onwards, the methane concentrations curves diverged, as methane was produced at a more rapid rate at 60 s than at 10 s. In contrast to methane, the ethane, ethylene and propane concentration–pressure plots at 10 and 60 s considerably diverged at a much higher pressure of 10 MPa.

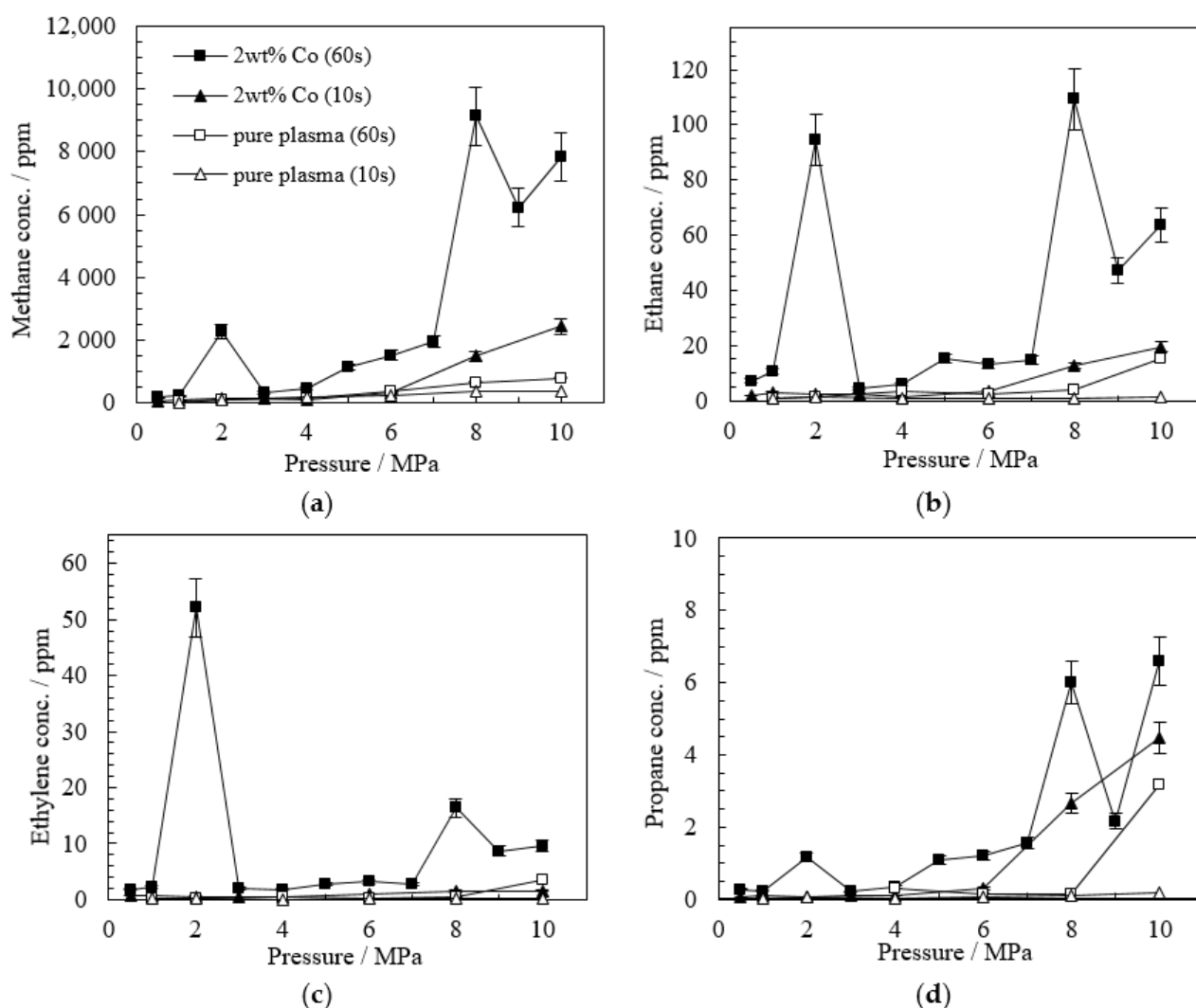


**Figure 1.** The influence of pressure on the hydrocarbon concentration for pure plasma and plasma-catalytic FTS (non-thermal plasma (NTP) + 2 wt% Co catalyst) at discharge times of 10 and 60 s: (a) methane, (b) ethane, (c) ethylene and (d) propane. Legend: ■—2 wt% Co (60 s); ▲—2 wt% Co (10 s); □—pure plasma (60 s); △—pure plasma (10 s). Operating conditions: syngas ( $H_2/CO$ ) ratio: 2.2:1; current: 350 mA; inter-electrode gap: 1 mm. Error bars (vertical): expanded experimental hydrocarbon concentration uncertainty of  $\pm 11\%$ .

These trends suggest that the extended treatment time of 60 s was more favourable for synthesis above 4 MPa. This concentration–pressure behaviour was attributed to the density gradients between the hot and the cold gases within the reactor. At higher pressures between 4 and 10 MPa, there were higher density gradients between the high temperature arc core and the ambient bulk gas. The increase in density gradients with increasing pressure would have led to greater convective forces thus leading to higher gas velocities and enhanced circulation of the surrounding bulk gas through the hot arc core, resulting in the treatment of greater quantities of the bulk gas. In contrast to higher pressures, at pressures  $\leq 4$  MPa for methane and  $\leq 2$  MPa for ethane, ethylene and propane, the lower density gradients caused poor gas mixing, leading to similar product concentrations for the 10 and 60 s treatment times, thus rendering the longer treatment time of 60 s to be ineffective. This was particularly evident at 2 and 4 MPa, where the methane concentration at 10 s surpassed that at 60 s.

The concentration–pressure plots for the more effective discharge period of 60 s, showed the following concentration trends between 4 and 10 MPa: ethane was relatively constant; ethylene and propane decreased between 4 and 8 MPa; methane increased by

over a factor of four. These results suggest that the pressure range of 4 to 8 MPa does not provide any advantage for the carbon chain growth, especially when considering the  $\pm 11\%$  experimental concentration uncertainty (represented by the vertical error bars in Figure 1 and estimated using the approach in Equation (4)).

The influence of pressure on hydrocarbon productions was evident at 10 MPa, as dramatic improvements in the  $C_2$  and  $C_3$  hydrocarbon concentrations were achieved. At 10 MPa, the maximum ethane (16.3 ppm), ethylene (3.4 ppm) and propane (2.8 ppm) concentrations were attained which were approximately 4, 9 and 20 times greater, respectively, than those produced at 8 MPa. In addition, propylene (1.2 ppm) was only detected at 10 MPa.

### 2.1.2. Plasma-Catalysis

The improvement in the hydrocarbon yields was clearly observed in plasma-catalysis using a 2 wt% Co catalyst (Figure 1a–d), which generally produced higher hydrocarbon yields at the shorter discharge time of 10 s compared to pure plasma at 60 s. These results suggest that Co catalyst was active for FTS.

For the plasma-catalytic study at 10 s, the methane, ethane, ethylene, and propane concentrations increased between 4 and 10 MPa—analogue to that for pure plasma at the same conditions but with higher overall concentrations. Another trend similar to pure plasma was that the longer discharge time of 60 s improved yields to a lesser degree between the moderate pressure range of 3 and 7 MPa, which was the case for pure plasma between 4 and 8 MPa. This suggests that the moderate pressure range does not provide any advantage for the carbon chain growth for plasma-catalytic FTS. An additional influence of the catalyst on FTS was seen in the significant increase in  $C_1$ – $C_3$  concentrations for plasma-catalysis at 8 MPa, compared to 10 MPa for the  $C_2$  and  $C_3$  hydrocarbons in pure plasma FTS, suggesting that the catalyst reduced the pressure required for chain growth in plasma-catalysis.

The most observable contrast between pure plasma and plasma-catalytic FTS was seen at 2 MPa. At 2 MPa, the methane concentration for pure plasma increased monotonically with pressure, whereas for plasma-catalysis, a local maximum existed for methane at 2 MPa, with either local maxima or maxima for ethane, ethylene and propane. The improvement at 2 MPa was so significant that at this pressure, the maximum ethylene yield (52 ppm) was obtained, and the ethane yield (95 ppm) was relatively close to the maximum yield obtained at 8 MPa (109 ppm). These results clearly indicate that the cobalt catalyst enhanced the reaction pathway and product selectivity of pure plasma FTS with the catalyst's influence being most prevalent at 2 MPa.

This result is interesting, as 2 MPa is a commonly used operating pressure in conventional FTS. The increase in hydrocarbon yields from 0.5 to 2 MPa was seen in the study by Zabidi et al. [45], who showed that an increase in pressure from 0.1 to 2 MPa led to an increase in the CO conversion of 60% (due to the fact of a higher reaction rate) and an increase in the  $C_{5+}$  selectivity of 57%.

The increase in  $C_1$ – $C_3$  hydrocarbon yields between the lower pressures of 0.5 and 2 MPa contrasted with the trend between 2 and 4 MPa, where a substantial decrease in the concentrations occurred (Figure 1a–d). Such a decline in  $C_1$ – $C_5$  hydrocarbon production between 2 and 4 MPa, observed by de la Pena O'Shea et al. [46], was attributed to the promotion of higher  $C_{6+}$  hydrocarbons as a result of higher pressures improving the solubility of  $H_2$  and CO. They also found that the increase in CO chemisorption with pressure enhanced particle segregation, which ultimately led to an increase in the active catalytic surface.

In addition to obtaining  $C_1$ – $C_3$  hydrocarbons, longer carbon chains were produced, but mainly in the form of carbonaceous species. These species were observed as a thin film of carbon deposits on the electrode surfaces, specifically on the conical cathode  $60^\circ$  tip and flat anode surface. Moreover, carbon deposits were seen on the catalyst. Carbon deposition

will be elaborated on in a follow-up paper that will investigate the effects of cobalt loading in plasma-catalytic FTS.

Furthermore, liquid water (visible as liquid droplets on the sight glass, and analysed using gas chromatography-mass spectrometry (GC-MS)), was exclusively produced between 8 and 10 MPa by plasma-catalytic FTS. High water yields are attributed to the presence of the cobalt catalyst, as in conventional FTS, where the water yields also increase with increasing operating pressure [47–50]. Due to the low water yields below 8 MPa in this study, water remained in the gaseous phase, whereas, between 8 and 10 MPa, water condensed, as a result of the higher yields and higher operating pressures.

Therefore, it could be observed in the current study that the longer treatment time of 60 s typically led to higher C<sub>1</sub>–C<sub>3</sub> hydrocarbon concentrations, a trend exhibited in both pure plasma and plasma-catalysis (as shown in Table 2). However, the concentration–pressure trends for plasma-catalysis at 60 s were more complex and deviated from that of pure plasma, in which the highest C<sub>2</sub> hydrocarbon yields were obtained at 2 MPa and 60 s. In addition, as presented in Table 2, the maximum propane yield of 6.6 ppm was achieved at 10 MPa and 60 s, with a comparable propane yield of 4.5 ppm at 10 MPa and 10 s. A chain growth indicator used to evaluate the pressure at which methane was a minimum (as methane is the least desired product), is the methane/ethane ratio (ratio of the two main products), presented in Table 2. As can be seen in Table 2, the lowest methane/ethane ratio of 24 was attained at 2 MPa, which was 5.1 times lower than the ratio at 10 MPa for the 60 s discharge time. In addition, the lowest ethane/ethylene ratio, representing the paraffin/olefin ratio was obtained at 2 MPa. This indicates that 2 MPa favoured olefin formation, desired in conventional FTS. Furthermore, at 2 MPa and 60 s, the plasma-catalytic methane, ethane, ethylene and propane concentrations of 2266, 95, 52 and 1.2 ppm, respectively, were 47, 68, 305 and 12 times higher than that of pure plasma.

**Table 2.** Hydrocarbon concentrations for the pure plasma and 2 wt% Co catalyst systems investigated at 1 and 10 MPa for a discharge time of 10 s and at 2 and 10 MPa for a discharge time of 60 s. (syngas (H<sub>2</sub>/CO) ratio: 2.2:1; current: 350 mA; inter-electrode gap: 1 mm; wall temperature: 25 °C; expanded experimental hydrocarbon concentration uncertainty: ±11%).

Product	Concentration/ppm							
	10 s				60 s			
	Pure plasma		Plasma-catalysis		Pure plasma		Plasma-catalysis	
1 MPa	10 MPa	1 MPa	10 MPa	2 MPa	10 MPa	2 MPa	10 MPa	
Methane	17	342	68	2428	48	772	2266	7836
	<i>C<sub>2</sub> hydrocarbons</i>							
Ethane	0.6	1.3	2.8	19	1.4	16	95	64
Ethylene	0.1	0.3	0.7	1.6	0.2	3.4	52	9.6
	<i>C<sub>3</sub> hydrocarbons</i>							
Propane	0.0	0.2	0.1	4.5	0.1	2.8	1.2	6.6
Propylene	0.0	0.0	0.0	0.0	0.0	1.2	0.0	0.0
	<i>Product ratio</i>							
Methane/ ethane	29	270	24	125	34	47	24	123
Ethane/ethylene	5.6	4.4	4.0	12.2	8.2	4.8	1.8	6.6

In addition to product yields, energy consumption was also determined for pure plasma and plasma-catalytic FTS. The voltage and current values were obtained from the digital oscilloscope used in this study and the variation of the voltage versus the operating pressure plots are presented in Figure 2a using the calculation method of Equation (5). The general trend for pure plasma and plasma-catalysis was that higher voltages were required at higher operating pressures for the electrical breakdown of syngas and ignition of the arc discharge.

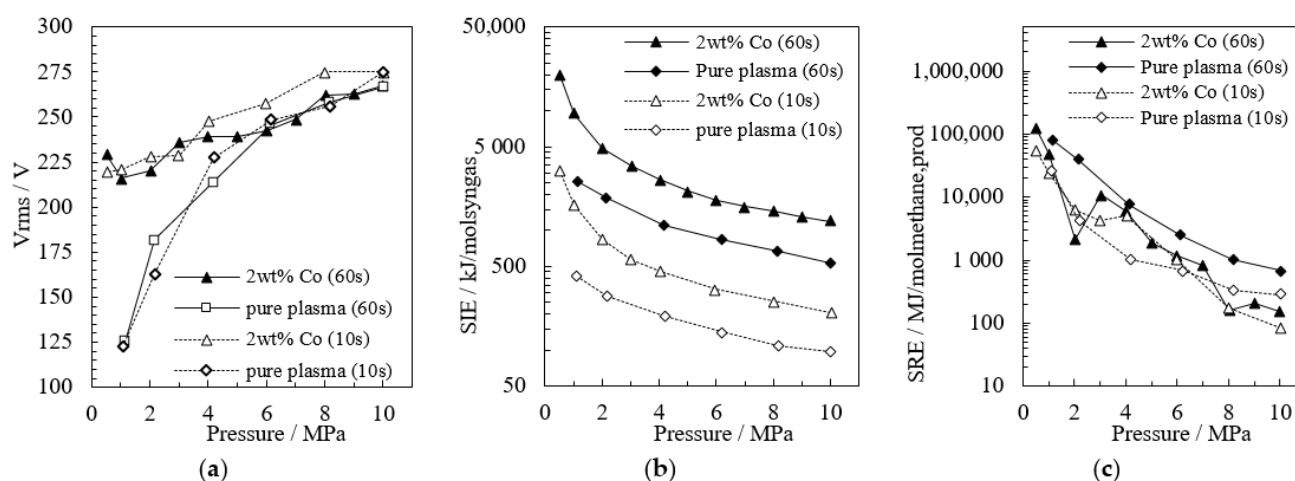


**Figure 2.** The influence of pressure on (a) discharge voltage, (b) specific input energy ( $\text{kJ/mol}_{\text{syngas}}$ ) and (c) specific required energy ( $\text{MJ/mol}_{\text{methane,prod}}$ ) for pure plasma FTS and plasma-catalytic FTS (NTP + 2 wt% Co catalyst) at discharge times of 10 and 60 s. Legend: ▲—2 wt% Co; ◊—pure plasma. Operating conditions: syngas ( $\text{H}_2/\text{CO}$ ) ratio: 2.2:1; current: 350 mA; inter-electrode gap: 1 mm; wall temperature: 25 °C.

The above-mentioned voltage–pressure behaviour was prevalent for both pure plasma and plasma-catalysis. However, the presence of the catalyst led to voltage deviations as seen in Figure 2a. Pure plasma required lower voltages than plasma-catalysis below 6 MPa. At 1 MPa, the pure plasma voltage of 125 V was 73% lower than that of plasma-catalysis (216 V). Between 1 and 6 MPa, the pure plasma voltage increased at a faster rate (121 V) than plasma-catalysis (27 V). The rapid voltage increase by more than two-fold for pure plasma between 1 and 6 MPa was probably a result of the reactor (syngas) volume exceeding double that of the plasma-catalytic volume, i.e., the presence of the catalyst reduced the reactor volume by approximately 54%. The larger volume for pure plasma inferred that greater density gradients existed between the hot arc and cold bulk gas, leading to a greater sensitivity of the pure plasma system to pressure variations. Hence, the comparatively steeper voltage–pressure curve for pure plasma. In contrast to the voltage–pressure behaviour below 6 MPa, pure plasma and plasma-catalysis required similar discharge voltages between 6 and 10 MPa as represented by the plateauing voltage–pressure curves in Figure 2a. Despite similar supply voltages, plasma-catalysis produced considerably higher hydrocarbon yields than pure plasma at both 10 and 60 s, suggesting that the cobalt catalyst was active for FTS and showcasing the plasma-catalytic synergistic effect.

In order to represent the electrical energy supplied per mole of syngas, the specific input energy, denoted as specific input energy (SIE) ( $\text{kJ/mol}_{\text{syngas}}$ ), was calculated using Equation (7) (Section 4.2.), in which the electrical energy consumption (E) was calculated using Equation (6). The SIE–pressure plots for pure plasma and plasma-catalysis are presented in Figure 2b. The increase in the SIE values and corresponding decrease in the hydrocarbon product yields at lower pressures for pure plasma and plasma-catalysis suggest that more energy was expended on bulk gas heating than on synthesis processes with an opposite trend at higher pressures.

The final factor considered for determining the energetic performance of FTS was the specific required energy, denoted as specific required energy (SRE) ( $\text{MJ/mol}_{\text{methane,prod}}$ ) and determined using Equation (8) (Section 4.2.). The observed trend for the SRE–pressure plots in Figure 2c reveals that less energy was required to produce methane at higher pressures for the 10 and 60 s studies, which in conjunction with the plateauing voltage–pressure curves between 8 and 10 MPa (Figure 2a), indicate that higher energy efficiency was achieved at higher pressures. The less energy required at higher pressures for methane formation could be explained by the more frequent electron–molecule collisions as a result

of shorter collisions paths at a higher pressure, which thus lead to a decrease in the energy required for reactant ( $H_2 + CO$ ) ionisation and dissociation, and chain growth processes.

For the 10 s study, the lowest SIE and SRE values and the maximum  $C_1$ – $C_3$  hydrocarbon yields for pure plasma and plasma-catalysis corresponded to the highest pressure of 10 MPa. Therefore, 10 MPa was considered the optimum operating pressure for the 10 s study, where plasma-catalysis was the most energy efficient system as determined by the SRE value of  $84 \text{ MJ/mol}_{CH_4,prod}$ , which was  $\sim 3.4$  times lower than pure plasma ( $284 \text{ MJ/mol}_{CH_4,prod}$ ).

For the 60 s study, the maximum  $C_2$  yields for plasma-catalysis were obtained at 2 MPa, corresponding to an SRE value of  $2148 \text{ MJ/mol}_{CH_4,prod}$ , which was  $\sim 18$  times lower than pure plasma ( $38\,961 \text{ MJ/mol}_{CH_4,prod}$ ). This was not the lowest SRE value for the 60 s study, which was attained at 10 MPa ( $152 \text{ MJ/mol}_{methane,prod}$ ). However, in view of improving chain growth and products yields for plasma–FTS research, a trade-off between chain growth, product yields and energy consumption favours 2 MPa as the optimal operating pressure for the 60 s experiments.

## 2.2. The Influence of Operating Current on Plasma-Catalytic FTS

In the current variation study, the supplied current ranged between 250 and 450 mA for a discharge time of 60 s, fixed inter-electrode gap of 1 mm and a fixed pressure of 2 MPa. The pressure of 2 MPa was selected for the present study as a low pressure permitted ignition and good stability of the arc discharge at the lower currents ( $<350 \text{ mA}$ ) in the current range studied. In addition to the arc stability, operating at 2 MPa (350 mA, 1 mm and 60 s) for the pressure variation study produced maximum concentrations of ethane and ethylene. The local maxima for methane and propane as well as the lowest methane/ethane and ethane/ethylene ratios were also observed at 2 MPa (350 mA, 1 mm and 60 s).

For pure plasma, an arc discharge was ignited at all supplied currents between 250 and 450 mA. The  $C_1$ – $C_3$  hydrocarbon yields shown in Figure 3a–d were usually higher at lower currents, where the maximum yields of methane (97 ppm), ethane (4 ppm), ethylene (14 ppm) and propane (0.3 ppm) were obtained at the minimum current of 250 mA. The methane yield obtained at 250 mA was double that of 350 mA (the fixed current for the pressure variation study). This trend occurred as the bulk gas and electrons at lower currents were further from thermal equilibrium, enabling electrons to focus their energy on plasma–chemical reactions instead of bulk gas heating. Greater bulk gas heating at higher currents were indicated by a greater increase in the bulk gas temperature ( $\Delta T$ ) of 3.86, 4.04, 5.09, 5.31 and  $5.62 \text{ }^\circ\text{C}$  at 250, 300, 350, 400 and 450 mA, respectively.

The concentration–current behaviour for plasma-catalysis was complex and deviated from the trend for pure plasma. The major deviation was that the maximum yields of methane (2266 ppm), ethane (95 ppm), ethylene (52 ppm) and propane (1.4 ppm) were achieved at 400 mA instead of 250 mA. Thus, FTSs at lower currents were less effective for plasma-catalysis.

The differing plasma-catalytic concentration–current behaviour cannot be ascribed to an irregularity in the supply voltage as both pure plasma and plasma-catalysis displayed similar voltage–current trends as shown in Figure 4a. However, the differing (and almost reverse) trend may have arisen from plasma-catalysis producing carbonaceous species, which were seen on the cathode tip and anode surfaces and detected on the catalyst surface. The influence of these electrically conductive carbonaceous species [51] are not clearly understood but may have modified the non-equilibrium nature of the plasma, especially at lower currents.

The decreasing voltage–current characteristic curves for pure plasma and plasma-catalysis (shown in Figure 4a) corresponded to that of a conventional non-thermal arc discharge ignited at high pressure [16,52,53], which was expressed by Ayrton’s empirical formula in which the voltage drop is a function of the supply current and inter-electrode gap [52].

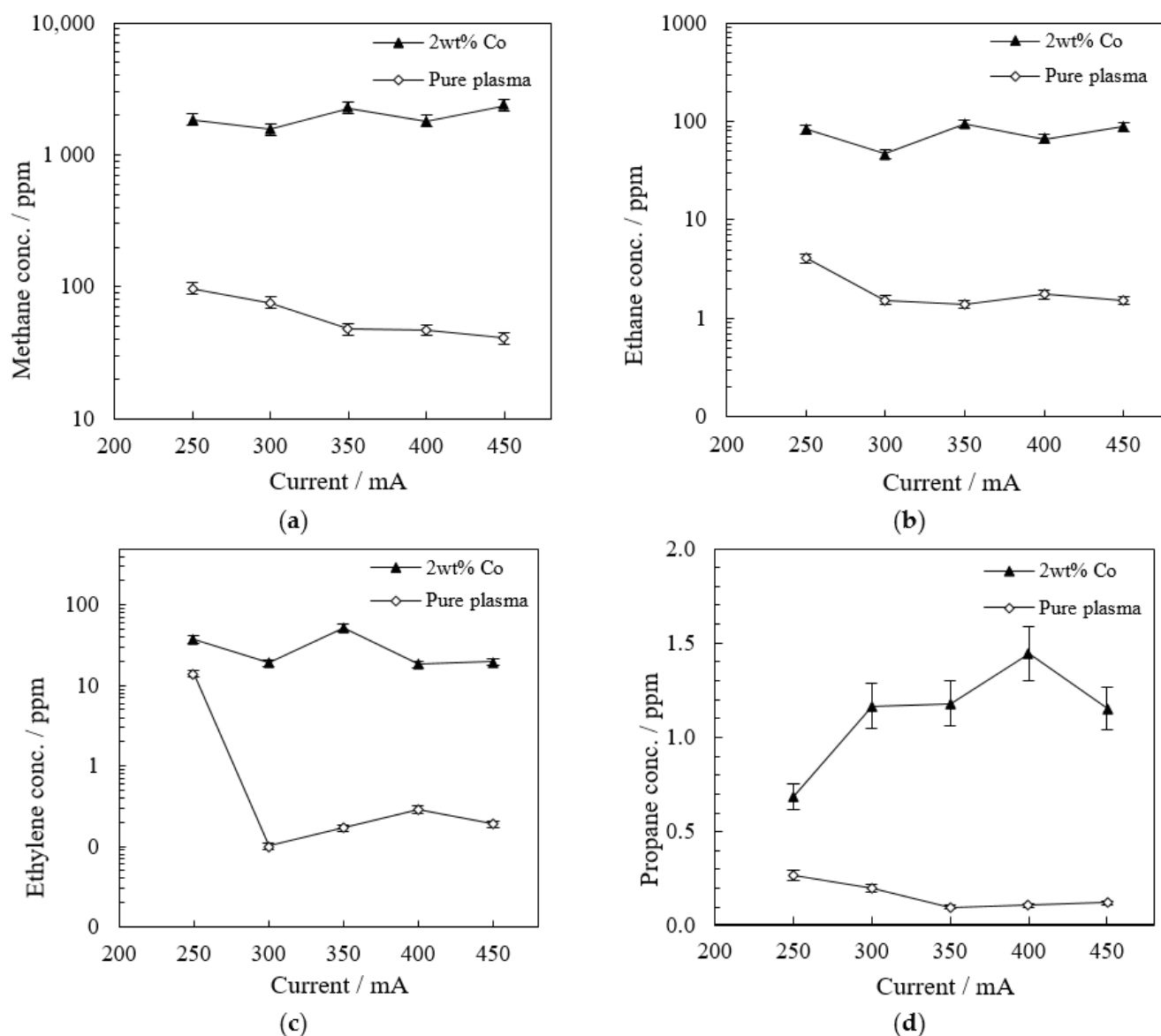


**Figure 3.** The influence of current on hydrocarbon concentration for pure plasma and plasma-catalytic FTS (NTP + 2 wt% Co catalyst) at a discharge time of 60 s: (a) methane, (b) ethane, (c) ethylene and (d) propane. Legend: ▲—2 wt% Co; ◇—pure plasma. Operating conditions: syngas ( $H_2/CO$ ) ratio: 2.2:1; pressure: 2 MPa; inter-electrode gap: 1 mm; wall temperature: 25 °C. Error bars (vertical): expanded experimental hydrocarbon concentration uncertainty of  $\pm 11\%$ .

The decrease in voltage also produced an increase in the electric field energy and SIE with increasing current, shown in Figure 4b. The increase in the SIE is an indication that more energy is deposited into the system per mole of syngas as the current increases. A high increase in the SIE could cause the plasma properties to be closer to a thermal arc state, where a substantial quantity of energy could be used for heating the bulk gas mixture, and where a much lower fraction of the discharge energy is transferred from the plasma in the syngas for reactant conversion.

This thermal state behaviour could probably explain the reduction in hydrocarbon yields with increasing current as seen in the concentration–current plots in Figure 3a–d, which was also related to the increase in the SIE with current. Similar to the pressure variation study, the SIE values for pure plasma were lower than that of plasma-catalysis as a result of the reduced reactor volume caused by the catalyst’s presence.

In the current variation study, the specific required energy (SRE) value of 2343 MJ/mol<sub>methane,prod</sub> at 250 mA for plasma-catalysis, shown in Figure 4c, was ~4.9 times

lower than that of pure plasma (11,483 MJ/mol<sub>methane,prod</sub>), suggesting that 250 mA was the most favourable operating current for hydrocarbon production and energy consumption.

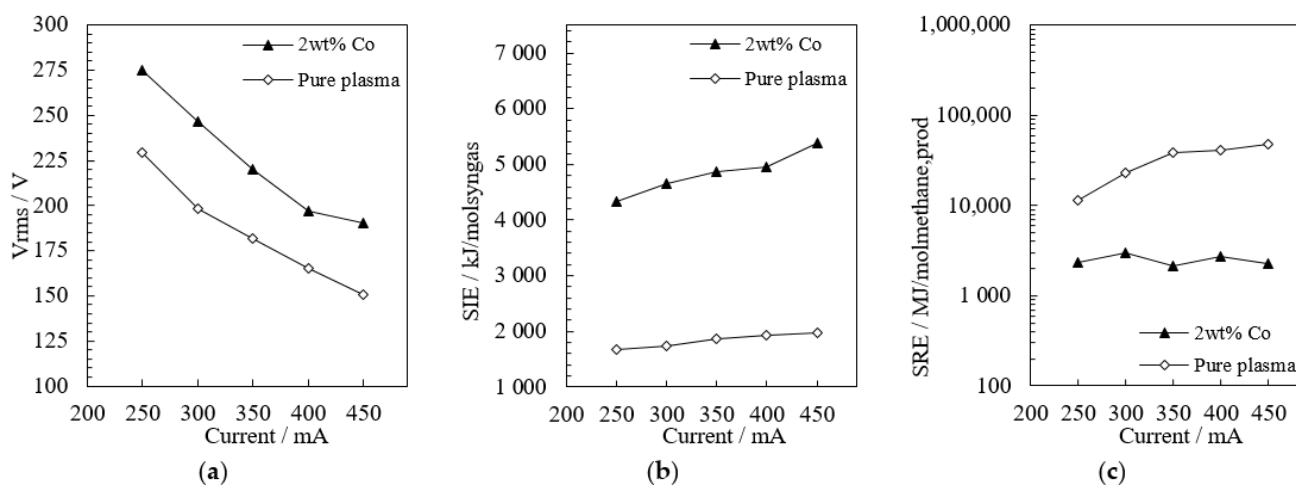


**Figure 4.** The influence of current on (a) discharge voltage, (b) specific input energy (kJ/mol<sub>syngas</sub>) and (c) specific required energy (MJ/mol<sub>methane,prod</sub>) for pure plasma and plasma-catalytic FTS (NTP + 2 wt% Co catalyst) at a discharge time of 60 s. Legend: ▲—2 wt% Co; ◇—pure plasma. Operating conditions: syngas (H<sub>2</sub>/CO) ratio: 2.2:1; pressure: 2 MPa; inter-electrode gap: 1 mm; wall temperature: 25 °C.

### 2.3. The Influence of the Inter-Electrode Gap on Plasma-Catalytic FTS

An increase in the inter-electrode gap from 0.5 to 2 mm at a fixed pressure of 2 MPa, fixed current of 350 mA and discharge period of 60 s generally led to an increase in hydrocarbon yields, as shown in Figure 5a–d. These fixed conditions were employed as they were the optimum conditions for production in the pressure variation study.

The expansion of the inter-electrode gap meant an increase in the arc column length and the volume of treated syngas. For an inter-electrode increase from 0.5 to 2 mm, the methane (15,202 ppm), ethane (352 ppm), ethylene (121 ppm) and propane (20 ppm) concentrations (at 2 mm) for plasma-catalysis increased by factors of approximately 6.4, 4.2, 4.4 and 14, respectively. In contrast, the methane yield for pure plasma increased by a lower factor of 5, whereas ethane was below 3 ppm and ethylene and propane yields were below 1 ppm (not shown in Figure 5b–d). These results indicate that the inter-electrode gap had a more significant influence on hydrocarbon production for plasma-catalysis than pure plasma, which was attributed to the differences in the active volumes of both systems.

For pure plasma FTS, a four-fold increase in the inter-electrode gap (from 0.5 to 2 mm) corresponded to a four-fold increase in the arc discharge volume, based on the assumption of a linear gap–volume relationship. However, for plasma-catalysis, a four-fold increase in the inter-electrode gap caused a four-fold increase in both the arc discharge volume and cobalt catalytic surface area exposed to the arc discharge, which were compounded to increase the catalytic activity and improve the overall FTS performance. This behaviour was corroborated at the widest discharge gap of 2 mm, where methane, ethane, ethylene and propane concentrations for the plasma-catalysis were factors of 154, 143, 331 and 340 times higher, respectively, than that obtained for pure plasma.

An increase in the inter-electrode gap from 0.5 to 2 mm, at a fixed pressure of 2 MPa, current of 350 mA and discharge time of 60 s, led to an increase in the supply voltage as shown in Figure 6a. The voltage increase ensured a sustainable arc discharge. The increasing voltage–gap behaviour was related to the influence of the inter-electrode gap on the thicknesses of the different zones constituting an arc discharge [45,54]: the near-cathode and near-anode border regions (closer to non-equilibrium) and positive arc column (further from non-equilibrium due to the fact of its higher intrinsic electrical resistivity).

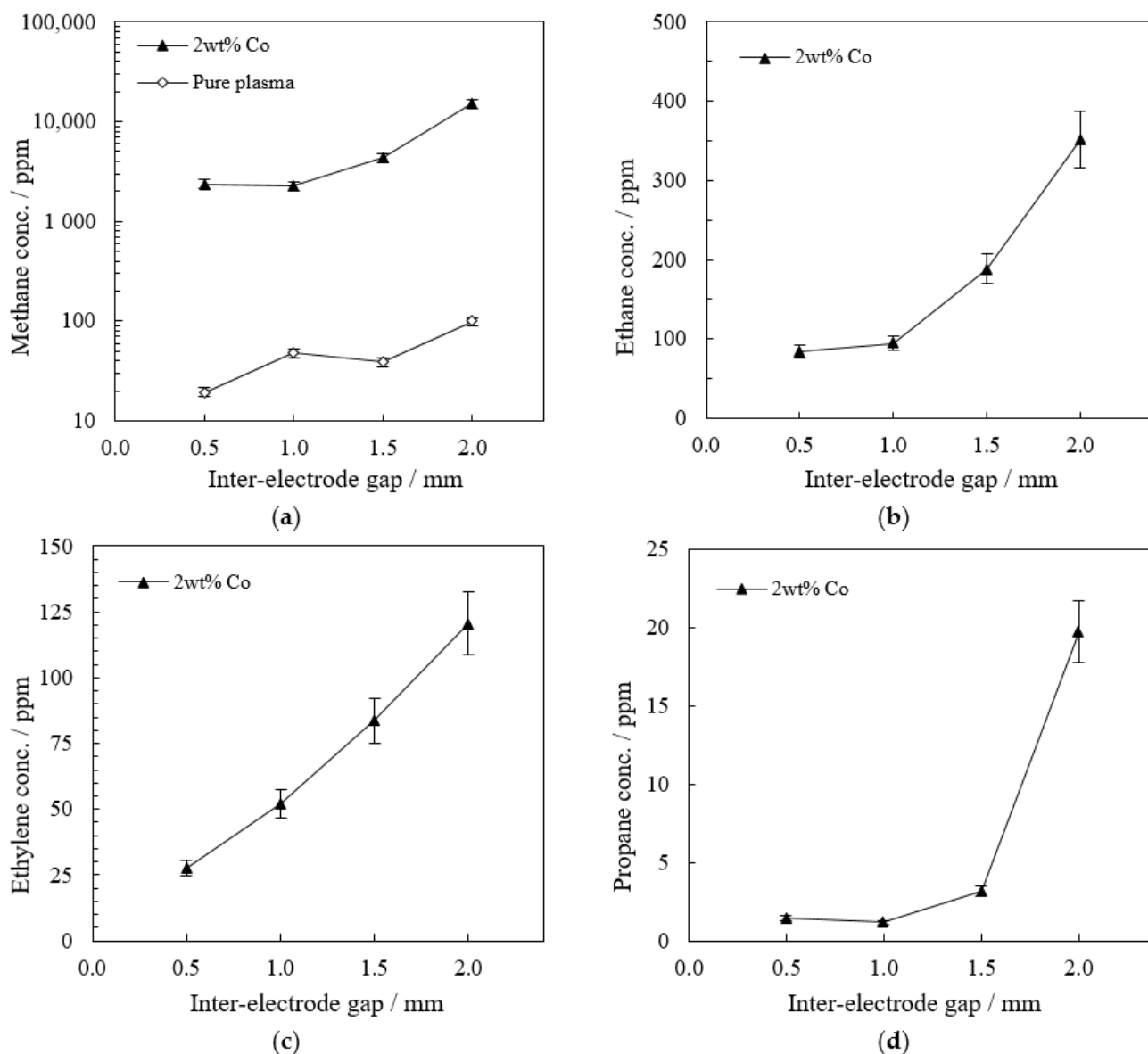


**Figure 5.** The influence of the inter-electrode gap on the hydrocarbon concentration for pure plasma and plasma-catalytic FTS (NTP + 2 wt% Co catalyst) at a discharge time of 60 s; (a) methane, (b) ethane, (c) ethylene and (d) propane. Legend: ▲—2 wt% Co; ◇—pure plasma. Operating conditions: syngas ( $H_2/CO$ ) ratio: 2.2:1; pressure: 2 MPa; current: 350 mA; wall temperature: 25 °C. Error bars (vertical): expanded experimental hydrocarbon concentration uncertainty of  $\pm 11\%$ .

A wider inter-electrode gap, 2 mm in this study, led to the formation of an elongated positive arc column with higher electrical resistivity that produced a more thermal plasma with greater convective losses. In order to maintain these thermal processes, a comparatively high supply voltage of 275 V was required for pure plasma as shown in Figure 6a. In contrast to the wider inter-electrode gaps, for a shorter discharge gap of 0.5 mm in this study, the non-equilibrium cathode and anode border zones controlled the electrical behaviour of the arc discharge, leading to a lower supply voltage requirement of 67 V for pure plasma as shown in Figure 6a. This arc discharge gap/zone behaviour also extended to plasma-catalysis: 141 V at 0.5 mm and 232 V at 2 mm. In addition to the arc discharge zones, the higher SIE values at wider discharge gaps, shown in Figure 6b, also suggest that the plasma was further from non-equilibrium.

The SRE values, presented in Figure 6c, decreased considerably from 0.5 to 2 mm for plasma-catalysis, revealing 1.5 to 2 mm as the optimal inter-electrode gap range in terms of

hydrocarbon yields and energy efficiency. At 2 mm, the SRE value of  $224 \text{ MJ/mol}_{\text{methane,prod}}$  for plasma-catalysis was approximately 126 times lower than that of pure plasma ( $28,207 \text{ MJ/mol}_{\text{methane,prod}}$ ).

A photograph of a typical arc discharge generated in the reactor for a mixture of hydrogen and carbon monoxide (syngas) at about 2 MPa with an inter-electrode gap of 1.25 mm is shown in Figure 7. This arc discharge has been shown to have a relatively low bulk gas temperature not higher than  $30^\circ\text{C}$ , while the temperature at the arc core is greater than 1 eV [15,52,55].

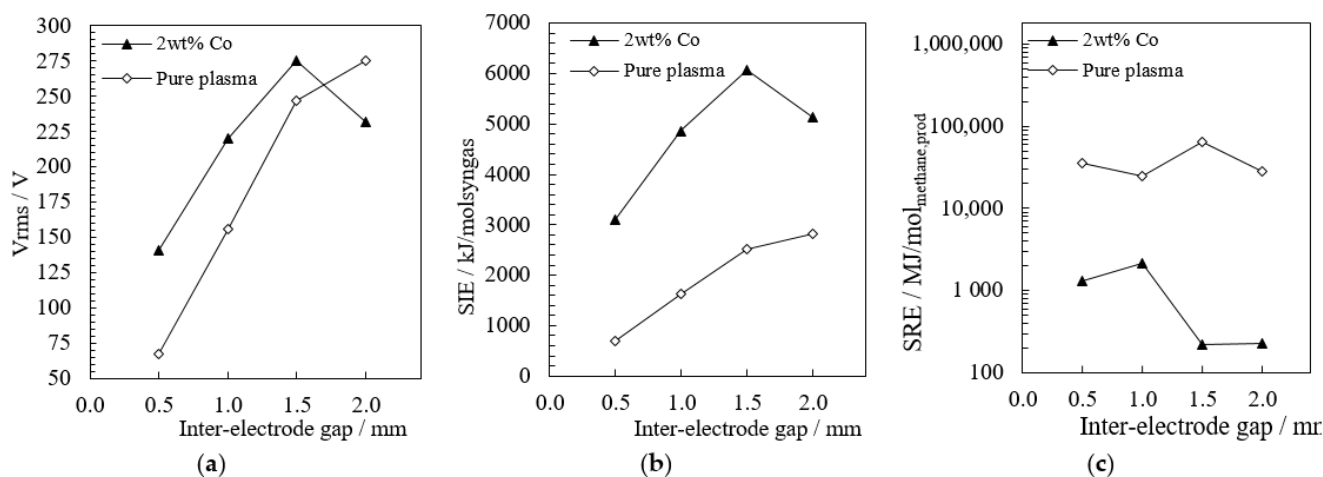


**Figure 6.** The influence of inter-electrode gap on (a) discharge voltage, (b) specific input energy ( $\text{kJ/mol}_{\text{syngas}}$ ) and (c) specific required energy ( $\text{MJ/mol}_{\text{methane,prod}}$ ) for pure plasma and plasma-catalytic FTS (NTP + 2 wt% Co catalyst) at a discharge time of 60 s. Legend: ▲—2 wt% Co; ◇—pure plasma. Operating conditions: syngas ( $\text{H}_2/\text{CO}$ ) ratio: 2.2:1; pressure: 2 MPa; current: 350 mA; wall temperature:  $25^\circ\text{C}$ .

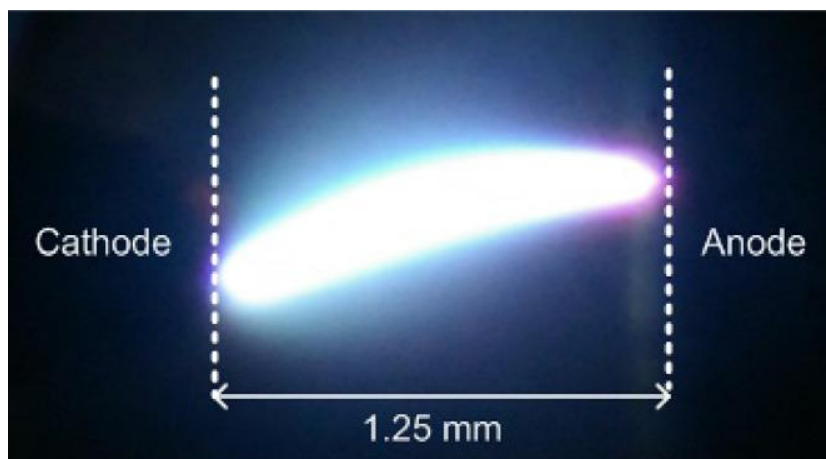


**Figure 7.** Photograph of the arc discharge generated between the interelectrode gap of 1.25 mm for a gas mixture  $\text{He}/\text{H}_2/\text{CO}$ : (40%/48%/12%); pressure: 2.25 MPa; current: 350 mA [15].

#### 2.4. Catalyst Characterisation

In order to further understand the effects of plasma on the catalyst and their related interactions, the catalyst was characterised using scanning electron microscopy (SEM) and energy-dispersive X-ray spectroscopy (EDX). The SEM micrographs shown in Figures 8 and 9 were captured at a magnification of up to 30,000 using the SmartSEM image capture software.

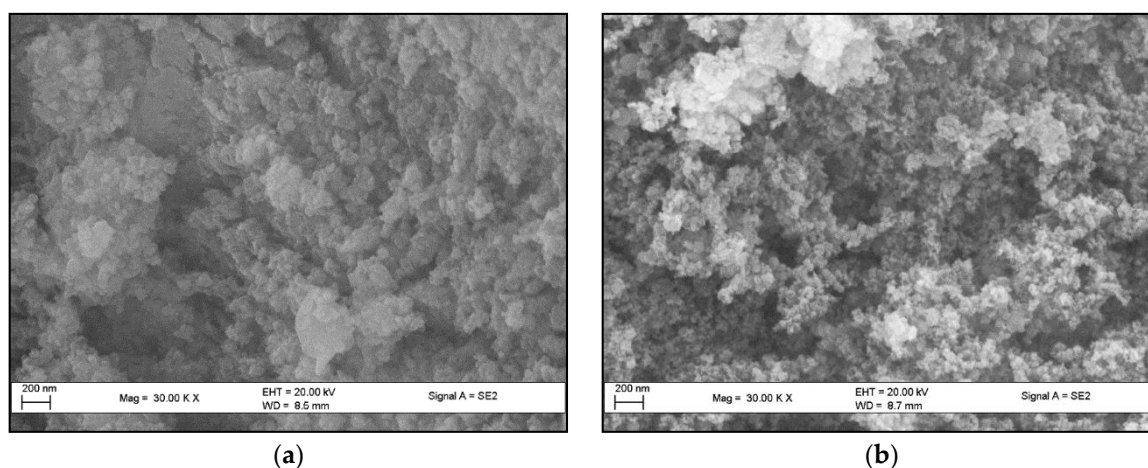


**Figure 8.** SEM micrographs of 2wt% Co catalysts: (a) fresh catalyst, (b) used catalyst.

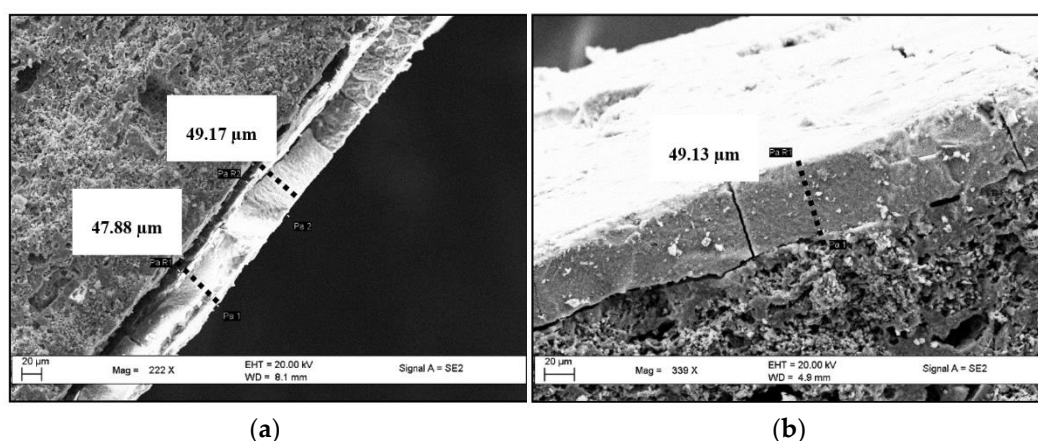


**Figure 9.** SEM images of catalyst coating thickness of the 2 wt% Co; (a,b).

#### 2.4.1. Scanning Electron Microscopy (SEM)

Scanning electron microscopy was employed to determine the catalyst surface characteristics. The SEM images of the inner cylindrical surfaces of the 2wt% Co catalyst, shown in Figure 8, illustrate the difference between the fresh and used catalysts. Larger cobalt clusters were visible on the fresh (calcined/reduced) 2 wt% Co catalyst (Figure 8a), while smaller and more highly dispersed clusters were seen on the used 2 wt% Co catalyst (Figure 8b).

The interaction between the active plasma species and the catalyst surface, as well as the high-pressure environment were both responsible for the catalyst's modification. In conventional FTS using a Co/SiO<sub>2</sub> catalyst, a similar increase in cobalt particle dispersion was observed for an increase in pressure from 2 to 4 MPa, in turn, producing more dispersed cobalt particles than those activated with pure H<sub>2</sub> [46]. The authors attributed the high dispersion to stronger CO chemisorption with increasing pressure, leading to the segregation of cobalt clusters and an increase in the active cobalt's surface area.

In addition to high-pressure operation, particle dispersion in the present study could have also been promoted by the pre-dissociated CO plasma species, which may have reduced the unreduced Co oxides to smaller Co metal particles, a phenomenon reported in other plasma-catalytic studies [14,30,31,56].

Furthermore, the scanning electron microscopy (SEM) was used to determine the catalyst coating thickness aside from the surface topography presented in Figure 8. The SEM micrographs in Figure 9 revealed the coating thicknesses of the used cobalt catalysts. The wash-coat layer thicknesses, measured at 20 different locations for the 2 wt% Co used

catalysts, ranged between 34 and 67  $\mu\text{m}$ , with an average coating thickness of 49  $\mu\text{m}$ . Hence, the main difference between Figure 9a,b is the different locations from which the measurement was taken in order to show that the catalyst was relatively uniform in its coating onto the surface of the support material. The coating thickness is important in continuous monolith reactors where mass transfer limitations are directly affected by the diffusion length (i.e., coating thickness) [57], which was not as significant for the batch process in this work.

#### 2.4.2. Energy-Dispersive X-ray Spectroscopy (EDX)

The SEM-EDX elemental mapping images of the coating thickness for the used 2 wt% Co catalyst are presented in Figure 10. The images showed the distinction between the mullite substrate (72 wt%  $\text{-Al}_2\text{O}_3/\text{SiO}_2$ ) and  $\gamma\text{-Al}_2\text{O}_3/\text{Co}$  coating layer. These images reveal that the cobalt particles were uniformly dispersed on the catalyst surface, which was most likely enhanced by plasma interactions as described in Section 2.4.1.

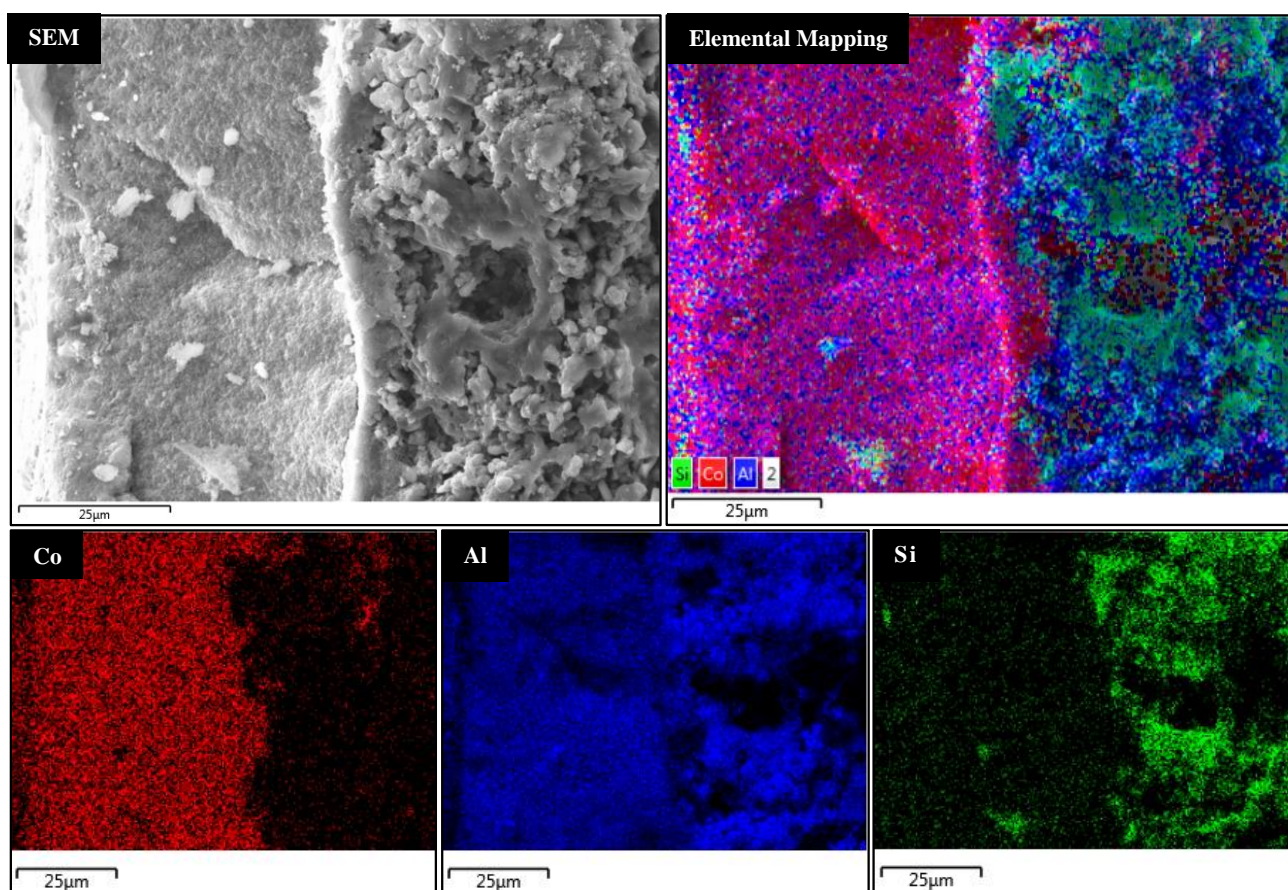


**Figure 10.** EDX elemental mapping analysis of the coating thickness for the used 2 wt% cobalt catalyst.

In addition to the EDX elemental mapping analysis of the coating thickness, semi-quantitative elemental composition analysis was performed using the energy-dispersive X-ray spectroscopy (EDX). Energy-dispersive X-ray spectroscopy can be reliably used for an analysis depth of up to 1000 nm. However, should the surface depth be about 10 nm, then the X-ray photoelectron spectroscopy will be preferred. The surface depth for the 2 wt% catalyst in this study was greater than 1000 nm. As shown in Figure 11, Al, Si and Co were the main elements present on the inspected surface of the coated mullite substrate, with Al being the most abundant element. The EDX elemental mapping for Al, Si and Co, within the inspection field, are indicated by unique colours on Figure 11.

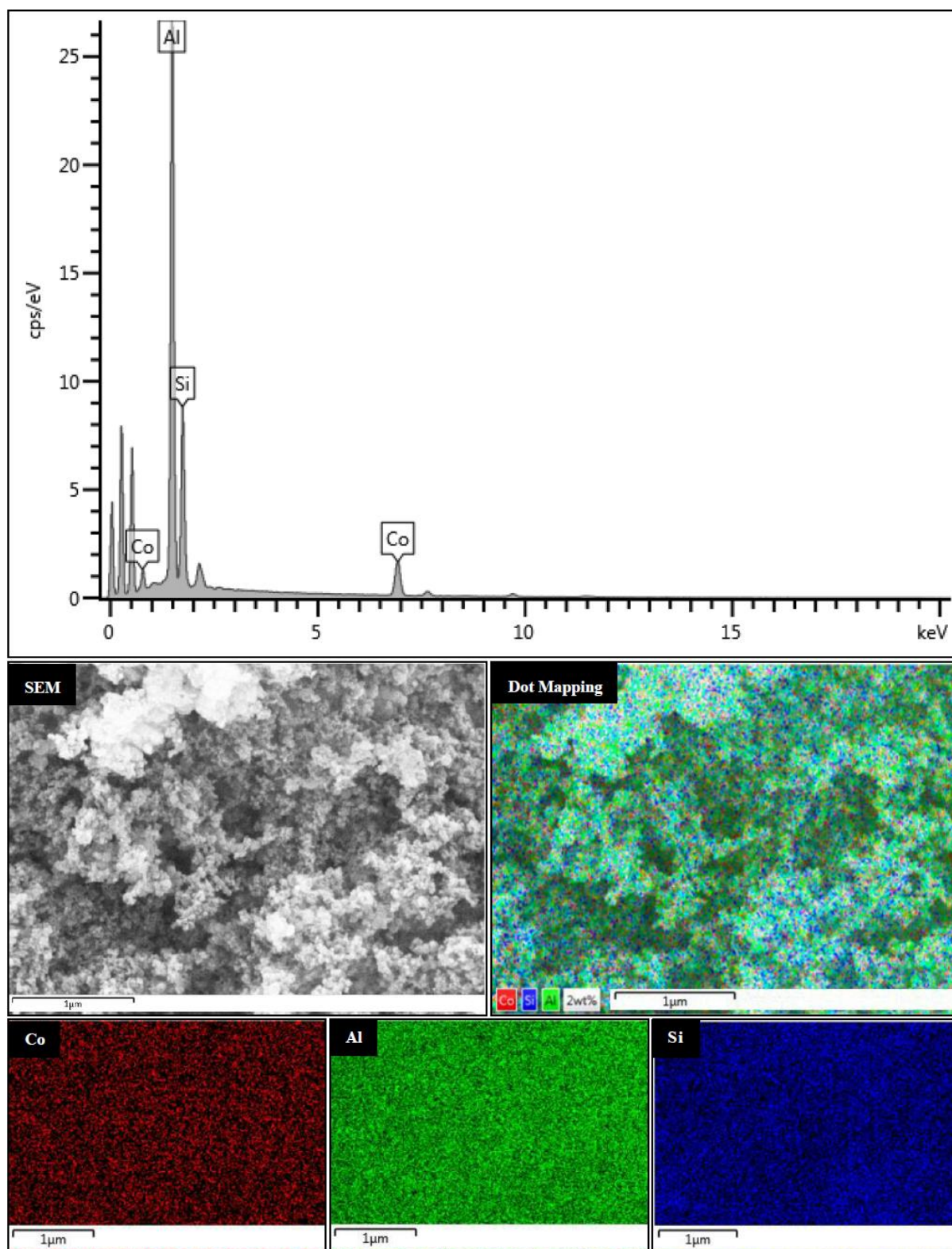


**Figure 11.** EDX dot mapping analysis of the surface of a used 2 wt% Co catalyst.

### 2.5. Plasma–Catalyst Interactions

From the present study, hydrocarbon synthesis using plasma-catalysis was presumed to occur via several possible reaction pathways: (i) plasma-chemical reactions originated in the hot arc core as in pure plasma FTS, in which methanation was the dominant reaction;

(ii) catalytic surface reactions (involving ground state CO and H<sub>2</sub> molecules), induced by plasma-heating of the catalyst, similar to catalytic thermal activation in classical (pure catalytic) FTS; (iii) catalytic surface reactions induced through plasma-dissociated CO and H<sub>2</sub> species (as radicals or in an excited state), interacting with the catalyst at close to ambient temperature, as seen in atmospheric pressure NTPs such as a dielectric barrier (DBD) and corona discharges.

The latter two catalytic reactions proposed were supported by the SEM analysis in Section 2.4.1, which showed that the plasma readily interacted with the catalyst. Furthermore, the product distribution for plasma-catalytic FTS resembled that of pure plasma FTS, especially with methane being the main product. This could imply that the general plasma-catalytic reaction scheme was mainly governed by the active plasma species during the relatively brief treatment periods of 10 and 60 s, i.e., plasma-chemical reactions were rapid compared to slower catalytic surface reactions. Catalytic reactions usually benefit from much longer residence periods, where the time-on-stream for optimal production in lab-scale and industrial FTS ranges from several hours up to weeks [58]. However, despite the high methane content for plasma-catalysis, the catalyst was clearly active for FTS as shown by the significant increases in the C<sub>1</sub>–C<sub>3</sub> hydrocarbon production rate and electrical energy efficiency.

### 3. Discussion

In the pure plasma and plasma-catalytic FTS experiments, C<sub>1</sub>–C<sub>3</sub> hydrocarbons were produced in the decreased order: methane >> ethane > ethylene > propane > propylene. High methane yields in plasma-catalysis suggest that plasma-chemical reactions occurred more rapidly than typically slower catalytic surface reactions. However, plasma-catalysis led to higher C<sub>1</sub>–C<sub>3</sub> hydrocarbons yields, olefinicity and energy efficiencies (lower specific required energy) than those of pure plasma. These results indicate that the 2 wt% Co/Al<sub>2</sub>O<sub>3</sub> catalyst enhanced the reaction pathway of pure plasma FTS and promoted C<sub>2</sub> and C<sub>3</sub> chain growth. This enhancement was attributed to the thermal activation of the catalyst (as in conventional FTS) by plasma-heating and/or by interaction with vibrationally-excited CO and radicals (as in atmospheric-pressure plasma-catalytic applications).

For plasma-catalysis, high C<sub>2</sub> and C<sub>3</sub> hydrocarbon yields, low methane/ethane and ethane/ethylene ratios, and low energy consumption—the optimum performance factors—were achieved at the following conditions: (i) 10 MPa at 10 s, 2 MPa at 60 s (favourable for C<sub>2</sub> hydrocarbon production), and 10 MPa at 60 s (favourable for propane production), for the pressure variation study (0.5 to 10 MPa); (ii) 250 mA for the current variation study (250 to 450 mA), due to this relatively low current generating a more non-equilibrium plasma state; (iii) an inter-electrode gap of 2 mm as a result of an increase in the reactive discharge zone and probably an increased activated catalytic surface. Therefore, the results indicated that the inter-electrode gap was the most influential operating parameter on product yields, chain growth and energy consumption, followed by current and pressure, which can be additionally optimised.

For the inter-electrode gap study at the widest gap of 2 mm (largest arc discharge volume and greatest surface area for catalytic heating), the methane (15,202 ppm), ethane (352 ppm), ethylene (121 ppm) and propane (20 ppm) concentrations for plasma-catalysis were factors of 154, 143, 331 and 340 times higher, respectively, than that obtained for pure plasma. Furthermore, the SRE value of 224 MJ/mol<sub>methane,prod</sub> for plasma-catalysis at 2 mm was approximately 126 times lower than that of pure plasma (28,207 MJ/mol<sub>methane,prod</sub>). Due to the highest yields and lowest SRE coinciding at 2 mm, this value was considered the optimum inter-electrode gap for plasma-catalysis based on this study.

The SEM and EDX analyses revealed that the Co-catalyst surface was enhanced by plasma treatment (indicating strong plasma–catalyst interactions), producing a more uniform Co dispersion and possibly reducing cobalt oxides to metallic cobalt as a result of the reductive syngas environment coupled with high-pressure operation.

## 4. Materials and Methods

### 4.1. Plasma Reactor Setup

A high-pressure, low-current tip-to-plane arc discharge reactor was used to facilitate the FTS process. A schematic of the batch reactor and auxiliary equipment are presented in Figure 12. The discharge chamber was cylindrical with an inner diameter of 12.15 mm and length of 24.45 mm. Two tungsten electrodes, both with a diameter of 4 mm, were inserted axially into the reactor. The fixed cathode had a cone-shaped tip at a 60° angle and the mobile anode had a flattened tip. Two face-to-face borosilicate Pyrex™ sight glasses allowed visual observation of the arc discharge. The reactor was fitted with a thermocouple to measure the bulk gas temperature. A WIKA E-10 high-pressure transducer (0–25 MPa) (WIKA Instruments Pty Ltd., Durban, South Africa) was used to measure the reactor operating pressure. A cooling jacket, containing water as the cooling fluid, regulated the bulk gas temperature within the reactor.

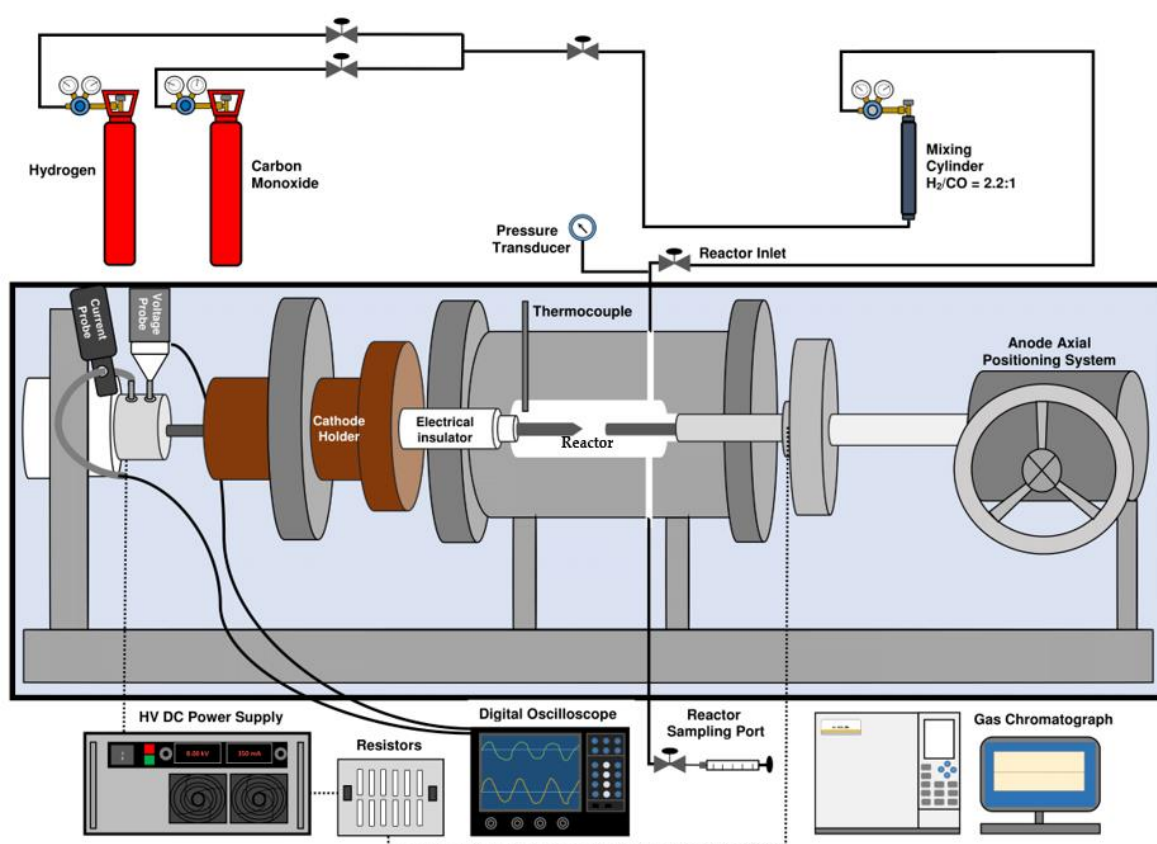


**Figure 12.** Schematic of the very high-pressure arc discharge reactor. HV: High Voltage, DC: Direct Current.

The cathode was connected to the negative polarity and the anode to the neutral point of the high voltage (HV) direct current (DC) power supply (Technix-SR-15-R-10,000 model (Technix, Créteil, France), with a maximum output voltage and current of 10 kV and 500 mA, respectively). As a safety measure, the power supply was connected in series to two 1 k $\Omega$  resistors that limited the output current. The power supply enabled the operator to fix the current while the voltage was automatically self-adjusted. More details of a similar power source and its electrical architecture were previously described in Reference [52].

In addition to the arc discharge reactor and power supply, the experimental setup incorporated a gas mixing vessel and reactor feed system, a gaseous products sampling port, and control and data (pressure, temperature, current and voltage) acquisition tools (as illustrated in Figure 12).

#### 4.2. Reactor Experimental Procedure.

The gases that constituted syngas, H<sub>2</sub> (99.999 mol%) and CO (99.999 mol%)—procured from Afrox (Durban, South Africa)—were mixed to achieve a H<sub>2</sub>/CO ratio of 2.2:1, which contained 15 ppm of methane as an impurity. The prepared syngas mixture was transferred to the discharge chamber of the reactor at the required operating pressure (between 0.5 and 10 MPa). The mobile electrode was moved axially towards the fixed electrode using an axial positioning system until contact of the electrodes was achieved, with continuity being verified using a multimeter. Direct contact of the electrodes was mandatory to overcome the limitations imposed by Paschen's Law under the low-current and high-pressure conditions.

Upon electrode contact, the high voltage DC power supply, set at the desired ignition current (between 250 and 450 mA) and ignition voltage (8 kV), was switched on. The arc was ignited immediately after the mobile electrode was retracted. When an inter-electrode gap width of 1 mm was attained, the reaction was allowed to proceed for a pre-determined time (10 or 60 s), after which period the power supply was switched off—immediately extinguishing the arc discharge.

After the power supply had been switched off, the valve at the outlet of the reactor was opened, and the reaction gaseous products were then withdrawn from the reactor at a sampling point into a 500 µL Hamilton<sup>®</sup> gastight syringe and analysed off-line by a Shimadzu<sup>™</sup> 2010 Plus gas chromatograph (GC) (Kyoto, Japan). The GC was fitted with a thermal conductivity detector (TCD) and flame ionisation detector (FID). The TCD, connected to a Supelco Carboxen 1000 (60/80) column, was calibrated to detect the permanent gases including CO and H<sub>2</sub>, and the FID, connected to a HP Al<sub>2</sub>O<sub>3</sub> PLOT column, was calibrated to detect C<sub>1</sub> to C<sub>3</sub> hydrocarbons. Table 3 gives the details of the columns and settings used on the GC for the analysis of the reactants and product gases.

**Table 3.** Gas chromatograph settings used in this work.

Analytes	Compound class	Channel 1	Channel 2
		Permanent gases H <sub>2</sub> , CO	Hydrocarbons CH <sub>4</sub> , C <sub>2</sub> H <sub>6</sub> , C <sub>2</sub> H <sub>4</sub> , C <sub>3</sub> H <sub>8</sub> , C <sub>3</sub> H <sub>6</sub>
Injector	Type	SPL-2010 (Direct mode)	SPL-2010 (Split mode)
	Carrier gas type	Nitrogen	Helium
	Carrier gas flow	30 mL·min <sup>-1</sup>	83 mL·min <sup>-1</sup>
	Temperature	250 °C	200 °C
	Split ratio	-	15:1
	Linear velocity	-	38.4 cm·s <sup>-1</sup>
	Gas volume injected	500 µL	500 µL
Column	Type	Packed	Capillary
	Make	Supelco	Hewlett-Packard
	Model	Carboxen 1000 (60/80)	Al <sub>2</sub> O <sub>3</sub> PLOT
	Length	4.5 m	30 m
	Inner diameter	2.10 mm	0.53 mm
	Film thickness	-	15 µm
	Maximum temperature	400 °C	200 °C
	Operating temperature	40 °C (Isothermal)	40 °C (10 min)–170 °C (ramp)
	Retention time	10 min	30 min
	Detector	Type	Thermal conductivity detector (TCD)
Temperature		275 °C	250 °C
Flame		-	35 mL·min <sup>-1</sup> H <sub>2</sub> 350 mL·min <sup>-1</sup> Air

Before the GC could be considered for the analysis of the reactants and product gases (after the plasma treatment), the Shimadzu 2010-plus GC (Kyoto, Japan) was calibrated using pure and diluted C<sub>1</sub>–C<sub>3</sub> hydrocarbon gases. The moles of gas injected into the GC by a syringe were determined by the ideal gas law equation. The errors incurred during the calibration process were assigned to the ideal gas parameters: pressure, volume, temperature and mole fraction of hydrocarbon species contained in the syringe. The calibration was undertaken at atmospheric pressure (measured using a barometer) and at ambient temperature (measured using a mercury thermometer).

The hydrocarbon product concentrations, reported in Section 2, were calculated by inserting the GC response data (acquired using the procedure described above), into the following equations:

$$x_i(\text{mols}) = (\text{GC Calibration slope})_i \times (\text{GC peak area})_i \quad (1)$$

$$C_i(\text{ppm}) = \left( \frac{x_i}{\sum_{i=1}^{\text{tot}} x_i + n_{\text{CO}} + x_{\text{H}_2}} \right) \times 1000\,000 \text{ ppm} \quad (2)$$

$$C_{i,\text{prod}}(\text{ppm}) = C_{i,\text{final}} - C_{i,\text{initial}} \quad (3)$$

where  $i$  represents the C<sub>1</sub>–C<sub>3</sub> hydrocarbon species,  $x_i$  denotes the number of moles,  $C_i$  denotes the concentration of species  $i$  present in the gas mixture prior to (*initial*) and after reaction (*final*), and  $C_{i,\text{prod}}$  is the concentration of species  $i$  produced by the reaction.

The expanded experimental uncertainty ( $U$ ) of  $\pm 11\%$  for  $C_{i,\text{prod}}$  was evaluated from the uncertainty contributions of two major error sources: sample measurement ( $u_{\text{rep}}$ ) and GC calibration ( $u_{\text{calib}}$ ).

$$U(\text{ppm}) = f(u_{\text{rep}}, u_{\text{calib}}) \approx \pm 11\% \quad (4)$$

The vertical error bars in the concentration versus operating parameter (pressure, current or inter-electrode gap) plots signify the expanded uncertainties.

In order to analyse the electrical energy performance of the reactor, a Chauvin Arnoux HX0027 (Asnières-Sur-Seine, France) high-voltage probe with a bandwidth between 0 and 100 kHz, and a Chauvin Arnoux E3N Hall-effect current probe with a bandwidth up to 100 kHz, were both connected to a LeCroy WaveJet 354-A digital oscilloscope (Teledyne LeCroy, Chestnut Ridge, NY, USA) with a bandwidth between 0 and 500 MHz. The oscilloscope recorded the voltage and the current signal for the 10 and 60 s treatment periods, respectively. The average of the voltage signal was utilised to determine the discharge voltage as shown in Equation (5).

$$U_{\text{avg}} = \sum_{i=1}^n \frac{(U_{\text{exp}})}{n} \quad (5)$$

where  $U$  is the voltage acquired by the oscilloscope, and  $n$  is the number of voltage values recorded: 10,000 at 10 s and 60,000 at 60 s. A similar approach was used for the current acquired by the oscilloscope.

The average voltage and current values, in addition, were used to evaluate the electrical energy consumption (SIE per mole of syngas and the SRE per mole of methane produced) using the following equations:

$$E (\text{kJ}) = U_{\text{avg}} I_{\text{avg}} \Delta t \quad (6)$$

$$\text{SIE}(\text{kJ}/x_{\text{syngas}}) = \frac{E}{x_{\text{syngas}}}, \text{ where } x_{\text{syngas}} = \frac{PV_{\text{reactor}}}{RT} \quad (7)$$

$$\text{SRE}(\text{kJ}/x_{\text{CH}_4,\text{produced}}) = \frac{E}{x_{\text{CH}_4,\text{after}} - x_{\text{CH}_4,\text{before}}} \quad (8)$$

where  $U_{avg}$  and  $I_{avg}$  are the average voltage and current, respectively;  $\Delta t$  is the discharge period of 10 or 60 s;  $E$  is the electrical energy supplied to generate the arc discharge;  $n_{syngas}$  is the moles of syngas, which is dependent on the universal gas constant ( $R$ ), and the syngas pressure ( $P$ ), reactor volume ( $V_{reactor}$ ) and (ambient) temperature ( $T$ ); finally,  $n_{CH_4}$  denotes the concentration of methane in the reactor before and after the discharge period.

The experimental apparatus and procedure and the calculation methods, described above, were employed for both the pure plasma and plasma-catalytic FTS studies, with a catalyst being integrated into the system for the plasma-catalysis study. A detailed description of the catalyst preparation and its configuration in the reactor are discussed in Section 4.3.

#### 4.3. Catalyst Configuration and Preparation

The industrially representative Co/Al<sub>2</sub>O<sub>3</sub> FTS catalyst could not be arranged in the arc discharge reactor according to the typical catalyst bed format used in atmospheric pressure in-plasma catalysis (IPC) [17,32,59–63] and post-plasma catalysis (PPC) [17,59,62] due to several factors: high temperature arc, low reactor volume (2.56 cm<sup>3</sup>), and intricate arrangement of the internal reactor components (particularly the electrodes and electrode holders).

The most suitable reactor–catalyst configuration was found to be that of the gliding arc discharge reactor [64,65], where the catalyst material was coated onto a ceramic substrate, which was positioned within close proximity to the discharge (but not in direct contact). This gliding arc catalyst configuration was combined with the catalyst coating technique used for monolithic (ceramic) catalysts [57,66–73], in order to produce a catalyst consisting of cobalt and  $\gamma$ -Al<sub>2</sub>O<sub>3</sub>, which were separately coated onto a pre-formed mullite substrate. Mullite was used as the catalyst substrate as it offered more suitable thermo-physical properties for this application [74–76]. The pre-formed LINE-OX<sup>®</sup> porous mullite (ceramic), fabricated by CERadvance Engineering Ceramics (CERadvance Engineering Ceramics Pty Ltd., Pretoria, South Africa), was composed of sintered 72 wt%-Al<sub>2</sub>O<sub>3</sub>/SiO<sub>2</sub> (porosity: 15%, bulk density: 2.7–2.8 g·cm<sup>-3</sup>, water absorption: 6–8%, modulus of rupture: 100 MPa, maximum temperature: 1400 °C, thermal conductivity: 5 W·m<sup>-1</sup>·K<sup>-1</sup>, thermal expansion at 1000 °C: 5.88 × 10<sup>-6</sup> °C<sup>-1</sup>).

The mullite substrate design ensured that the fixed and mobile electrodes were capable of axially contacting each other within the annulus of the catalyst, whilst avoiding direct contact of the electrodes and arc discharge with the catalyst's inner surface, as illustrated in Figure 13. The distance between the catalyst's inner surface and both electrodes' outer surfaces was approximately 1.5 mm, and the distance between the catalyst's surface and the conical tip of the cathode, where the arc was initiated, was approximately 3.5 mm. Additional catalyst design considerations included face-to-face perforations of 5 mm, which aligned with the circular windows of the reactor to allow visualization of the arc discharge; three cut-outs at the edges of the cylinder, each with a radius of 2.5 mm, which accommodated the thermocouple line; and reactor inlet and outlet (sampling) lines. Hence, the reactor configuration with the inserted catalyst support reduced the original total reactor volume (without a catalyst (2.56 cm<sup>3</sup>)) by 54% to 1.20 cm<sup>3</sup>.

In preparing the catalyst, the Cobalt and Al<sub>2</sub>O<sub>3</sub> were deposited separately as thin layers on the surface of a pre-formed LINE-OX<sup>®</sup> porous (72 wt%-Al<sub>2</sub>O<sub>3</sub>/SiO<sub>2</sub>) mullite substrate. Coating cobalt and Al<sub>2</sub>O<sub>3</sub> separately, compared to a single Co/Al<sub>2</sub>O<sub>3</sub> coat, led to a higher conversion and C<sub>5+</sub> selectivity in the pure catalytic FTS study by Bakhtiari et al. [57]. The coating process was a combination of the  $\gamma$ -Al<sub>2</sub>O<sub>3</sub> wash-coating method described by Villegas et al. [77], and the cobalt deposition method used for monolithic FTS catalysts [57,66,69,70,72,78].

For the  $\gamma$ -Al<sub>2</sub>O<sub>3</sub> layer, the  $\gamma$ -Al<sub>2</sub>O<sub>3</sub> powder (3  $\mu$ m average particle size supplied by Alfa-Aesar, Thermo Fisher (Kandel), Rheinland-Pfalz, Germany) was mixed with water to form a slurry (Al<sub>2</sub>O<sub>3</sub>/H<sub>2</sub>O = 25 wt%), with the addition of nitric acid, HNO<sub>3</sub> (HNO<sub>3</sub>/Al<sub>2</sub>O<sub>3</sub> = 2.2 mol·g<sup>-1</sup>), to aid alumina dispersion. The slurry was mixed by a magnetic stirrer for 15 h at room temperature. A ceramic substrate was then immersed vertically into

the prepared slurry for 15 min. After removing the precursor, the excess suspension was removed using a stream of compressed air. The precursor was dried in a static furnace at 600 °C for 15 min and weighed, with the coating process repeated until a target 5 wt% alumina wash-coat was achieved.

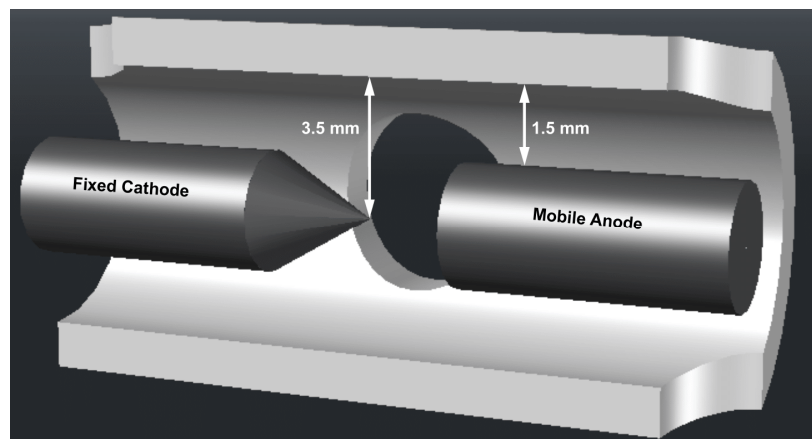


**Figure 13.** Cross-sectional isometric view of the LINE-OX<sup>®</sup> porous mullite substrate and electrodes.

The alumina wash-coated mullite substrate was then dipped into a cobalt nitrate hexahydrate  $\text{Co}(\text{NO}_3)_2 \cdot 6\text{H}_2\text{O}$  solution (Sigma–Aldrich Pty Ltd., Darmstadt, Germany) for 15 min; afterwards, the cobalt impregnated substrate was then dried in an oven at 120 °C for 60 min and weighed. The ceramic was then calcined in air at 450 °C for 4 h and reduced ex-situ at 350 °C for 3 h with 30 mL·min<sup>−1</sup> of pure H<sub>2</sub>. After reduction, the catalyst was weighed (2 wt%-Co) and immediately inserted into the reactor.

The prepared 2 wt%-Co/5 wt%- $\gamma$ -Al<sub>2</sub>O<sub>3</sub> mullite catalyst was then inserted into the discharge chamber of the reactor. The same catalyst was kept in the reactor for the entire period of investigation, which included the pressure, current and inter-electrode gap studies.

#### 4.4. Catalyst Characterisation

Scanning electron microscopy and energy-dispersive x-ray were used to characterise the 2 wt% Co/5 wt%-Al<sub>2</sub>O<sub>3</sub> mullite catalyst. A catalyst sample was prepared for SEM imaging by breaking the large coated mullite substrate into smaller fragments to fit onto the SEM stage. A single catalyst fragment was secured onto the stage using carbon tape. A thin film of gold was applied to the mounted sample using a Quorum Tech Q150RES sputter coater (Quorum Technologies, East Sussex, UK). Gold coating reduced the undesired electron charging effects experienced during the imaging process. The sample stage was then introduced to the microscope chamber, which was evacuated using a turbomolecular vacuum pump. This sub-atmospheric environment supported the transfer of electrons between the emission source and detector. A Zeiss Ultra Plus FEG instrument (Carl Zeiss AG, Oberkochen, Germany) was used to image the surfaces of the fresh and used catalysts. In addition to SEM analysis, SEM–EDX was used for elemental analysis of the catalyst. The EDX instrument was an Oxford X-Max 80 mm SDD (Oxford Instruments, High Wycombe, United Kingdom) with AZtecLive analysis software.

## 5. Conclusions

This study demonstrated that an arc discharge could be ignited and sustained at very high pressure in the presence of a catalyst, achieved by combining the wash-coating technique used in monolithic catalysis and a reactor–catalyst configuration employed in atmospheric pressure plasma-catalysis. This catalyst–reactor configuration should be transferable to other synthesis processes at high pressure within the regime of an electrical arc discharge.

Higher C<sub>1</sub>–C<sub>3</sub> hydrocarbons yields, olefinicity and energy efficiencies were observed for the plasma-catalytic process, with results indicating that the inter-electrode gap was the most influential operating parameter on product yields, chain growth and energy consumption, followed by current and pressure. Hence, the promising results from this study demonstrate the potential synergy between plasma and a conventional catalyst. Future research will extensively investigate catalyst characterisation of different catalyst loadings in FTS with a view of proposing possible reaction pathways for plasma–catalyst interactions.

**Author Contributions:** Conceptualization, B.B.G. and S.A.I.; methodology, B.B.G. and S.A.I.; validation, B.B.G., S.A.I. and D.R.; formal analysis, B.B.G.; investigation, B.B.G.; data curation, B.B.G.; writing—original draft preparation, B.B.G.; writing—review and editing, S.A.I.; supervision, S.A.I. and D.R.; funding acquisition, D.R. All authors have read and agreed to the published version of the manuscript.

**Funding:** This research was supported by the Department of Science and Technology (DST) and the National Research Foundation (NRF) through the South African Research Chair Initiative for Fluorine Process Engineering and Separation Technology present at the University of KwaZulu-Natal, South Africa at the time of the study.

**Institutional Review Board Statement:** Not Applicable.

**Informed Consent Statement:** Not Applicable.

**Data Availability Statement:** Data will be made available by authors on request.

**Acknowledgments:** The authors wish to thank the Microscopy and Microanalysis Unit (MMU) at the University of KwaZulu-Natal (South Africa) for the SEM–EDX.

**Conflicts of Interest:** The authors declare no conflict of interest.

## References

1. Takeshita, T.; Yamaji, K. Important roles of Fischer–Tropsch synfuels in the global energy future. *Energy Policy* **2008**, *36*, 2773–2784. [[CrossRef](#)]
2. Morales, F.; Weckhuysen, B.M. Promotion Effects in Co-Based Fischer–Tropsch Catalysis. *Catalysis* **2006**, *19*, 1–40. [[CrossRef](#)]
3. Aranda, G.; van der Drift, A.; Smit, R. *The Economy of Large Scale Biomass to Substitute Natural Gas (bioSNG) Plants*; Report ECN-E-14-008; ECN: Petten, The Netherlands, 2014.
4. Lobo, P.; Hagen, D.E.; Whitefield, P.D. Comparison of PM Emissions from a Commercial Jet Engine Burning Conventional, Biomass, and Fischer–Tropsch Fuels. *Environ. Sci. Technol.* **2011**, *45*, 10744–10749. [[CrossRef](#)]
5. Schihl, P.; Hoogterp-Decker, L.; Gingrich, E. The Ignition Behavior of a Coal to Liquid Fischer-Tropsch Jet Fuel in a Military Relevant Single Cylinder Diesel Engine. *SAE Int. J. Fuels Lubr.* **2012**, *5*, 785–802. [[CrossRef](#)]
6. Wang, H.; Oehlschlaeger, M.A. Autoignition studies of conventional and Fischer–Tropsch jet fuels. *Fuel* **2012**, *98*, 249–258. [[CrossRef](#)]
7. Beyersdorf, A.; Timko, M.; Ziemba, L.; Bulzan, D.; Corporan, E.; Herndon, S.; Howard, R.; Miake-Lye, R.; Thornhill, K.; Winstead, E. Reductions in aircraft particulate emissions due to the use of Fischer–Tropsch fuels. *Atmos. Chem. Phys.* **2014**, *14*, 11–23. [[CrossRef](#)]
8. Best, L.M.; Ana, B.; Bradford, R.L.; Hepp, A.F. *Characterization of Catalyst Materials for Production of Aerospace Fuels*; NASA/TM—2012-217403; National Aeronautics and Space Administration: Washington, DC, USA, 2012.
9. Oukaci, R.; Singleton, A.H.; Goodwin, J.G. Comparison of patented Co F–T catalysts using fixed-bed and slurry bubble column reactors. *Appl. Catal. A Gen.* **1999**, *186*, 129–144. [[CrossRef](#)]
10. Rytter, E.; Holmen, A. Deactivation and Regeneration of Commercial Type Fischer-Tropsch Co-Catalysts—A Mini-Review. *Catalysts* **2015**, *5*, 478–499. [[CrossRef](#)]
11. Dry, M.E. The Fischer–Tropsch process: 1950–2000. *Catal. Today* **2002**, *71*, 227–241. [[CrossRef](#)]
12. Dry, M.E. Practical and theoretical aspects of the catalytic Fischer-Tropsch process. *Appl. Catal. A Gen.* **1996**, *138*, 319–344. [[CrossRef](#)]
13. Dry, M.E. High quality diesel via the Fischer-Tropsch process—A review. *J. Chem. Technol. Biotechnol.* **2002**, *77*, 43–50. [[CrossRef](#)]
14. Al-Harrasi, W.S.; Zhang, K.; Akay, G. Process intensification in gas-to-liquid reactions: Plasma promoted Fischer-Tropsch synthesis for hydrocarbons at low temperatures and ambient pressure. *Green Process. Synth.* **2013**, *2*, 479–490. [[CrossRef](#)]
15. Rohani, V.; Iwarere, S.; Fabry, F.; Mourard, D.; Izquierdo, E.; Ramjugernath, D.; Fulcheri, L. Experimental Study of Hydrocarbons Synthesis from Syngas by a Tip–Tip Electrical Discharge at Very High Pressure. *Plasma Chem. Plasma Process.* **2011**, *31*, 663–679. [[CrossRef](#)]

16. Iwarere, S.; Rohani, V.; Ramjugernath, D.; Fabry, F.; Fulcheri, L. Hydrocarbons synthesis from syngas by very high pressure plasma. *Chem. Eng. J.* **2014**, *241*, 1–8. [[CrossRef](#)]
17. Chen, H.L.; Lee, H.M.; Chen, S.H.; Chang, M.B.; Yu, S.J.; Li, S.N. Removal of Volatile Organic Compounds by Single-Stage and Two-Stage Plasma Catalysis Systems: A Review of the Performance Enhancement Mechanisms, Current Status, and Suitable Applications. *Environ. Sci. Technol.* **2009**, *43*, 2216–2227. [[CrossRef](#)]
18. Roland, U.; Holzer, F.; Kopinke, F.-D. Improved oxidation of air pollutants in a non-thermal plasma. *Catal. Today* **2002**, *73*, 315–323. [[CrossRef](#)]
19. Morent, R.; Dewulf, J.; Steenhaut, N.; Leys, C.; Van Langenhove, H. Hybrid Plasma-Catalyst System for the Removal of Trichloroethylene in Air. *J. Adv. Oxid. Technol.* **2006**, *9*, 53–58. [[CrossRef](#)]
20. Nikoo, M.K.; Sharifi, M.A.; Amin, N.S. Carbon dioxide reforming of methane by catalytic-plasma reactor over Cu/Zn/ $\gamma$ -Al<sub>2</sub>O<sub>3</sub>. *J. Teknol. Sci. Eng.* **2011**, *56*, 75–86.
21. Amouroux, J.; Cavadias, S.; Doubla, A. Carbon Dioxide reduction by non-equilibrium electrocatalysis plasma reactor. *IOP Conf. Ser. Mater. Sci. Eng.* **2011**, *19*, 012005. [[CrossRef](#)]
22. Eliasson, B.; Kogelschatz, U.; Xue, B.; Zhou, L.-M. Hydrogenation of Carbon Dioxide to Methanol with a Discharge-Activated Catalyst. *Ind. Eng. Chem. Res.* **1998**, *37*, 3350–3357. [[CrossRef](#)]
23. Li, M.-W.; Tian, Y.-L.; Xu, G.-H. Characteristics of Carbon Dioxide Reforming of Methane via Alternating Current (AC) Corona Plasma Reactions. *Energy Fuels* **2007**, *21*, 2335–2339. [[CrossRef](#)]
24. Wallis, A.E.; Whitehead, J.; Zhang, K. The removal of dichloromethane from atmospheric pressure air streams using plasma-assisted catalysis. *Appl. Catal. B Environ.* **2007**, *72*, 282–288. [[CrossRef](#)]
25. Nozaki, T.; Muto, N.; Kado, S.; Okazaki, K. Dissociation of vibrationally excited methane on Ni catalyst: Part 1. Application to methane steam reforming. *Catal. Today* **2004**, *89*, 57–65. [[CrossRef](#)]
26. Nozaki, T.; Muto, N.; Kadio, S.; Okazaki, K. Dissociation of vibrationally excited methane on Ni catalyst: Part 2. Process diagnostics by emission spectroscopy. *Catal. Today* **2004**, *89*, 67–74. [[CrossRef](#)]
27. Pietruszka, B.; Anklam, K.; Heintze, M. Plasma-assisted partial oxidation of methane to synthesis gas in a dielectric barrier discharge. *Appl. Catal. A Gen.* **2004**, *261*, 19–24. [[CrossRef](#)]
28. Liu, C.-J.; Vissokov, G.P.; Jang, B.W.-L. Catalyst preparation using plasma technologies. *Catal. Today* **2002**, *72*, 173–184. [[CrossRef](#)]
29. Guo, Y.F.; Ye, D.Q.; Chen, K.F.; He, J.C.; Chen, W.L. Toluene decomposition using a wire-plate dielectric barrier discharge reactor with manganese oxide catalyst in situ. *J. Mol. Catal. A Chem.* **2006**, *245*, 93–100. [[CrossRef](#)]
30. Zhang, Y.P.; Ma, P.S.; Zhu, X.; Liu, C.J.; Shen, Y. A novel plasma-treated Pt/NaZSM-5 catalyst for NO reduction by methane. *Catal. Commun.* **2004**, *5*, 35–39. [[CrossRef](#)]
31. Cheng, D.-G.; Zhu, X.; Ben, Y.; He, F.; Cui, L.; Liu, C.-J. Carbon dioxide reforming of methane over Ni/Al<sub>2</sub>O<sub>3</sub> treated with glow discharge plasma. *Catal. Today* **2006**, *115*, 205–210. [[CrossRef](#)]
32. Whitehead, J.C. Plasma catalysis: A solution for environmental problems. *Pure Appl. Chem.* **2010**, *82*, 1329–1336. [[CrossRef](#)]
33. Van Durme, J.; Dewulf, J.; Sysmans, W.; Leys, C.; Van Langenhove, H. Efficient toluene abatement in indoor air by a plasma catalytic hybrid system. *Appl. Catal. B Environ.* **2007**, *74*, 161–169. [[CrossRef](#)]
34. Tu, X.; Whitehead, J. Plasma-catalytic dry reforming of methane in an atmospheric dielectric barrier discharge: Understanding the synergistic effect at low temperature. *Appl. Catal. B Environ.* **2012**, *125*, 439–448. [[CrossRef](#)]
35. Gallon, H.J.; Tu, X.; Twigg, M.V.; Whitehead, J.C. Plasma-assisted methane reduction of a NiO catalyst—Low temperature activation of methane and formation of carbon nanofibres. *Appl. Catal. B Environ.* **2011**, *106*, 616–620. [[CrossRef](#)]
36. Bromberg, L.; Cohn, D.; Rabinovich, A.; Alexeev, N.; Samokhin, A.; Hadidi, K.; Palaia, J.; Margarit-Bel, N. *Onboard Plasmatron Hydrogen Production for Improved Vehicles*; Report PSFC JA-06-3; MIT Plasma Fusion and Science Center: Cambridge, MA, USA, 2006.
37. Chu, W.; Wang, L.-N.; Chernavskii, P.A.; Khodakov, A.Y. Glow-Discharge Plasma-Assisted Design of Cobalt Catalysts for Fischer-Tropsch Synthesis. *Angew. Chem. Int. Ed.* **2008**, *47*, 5052–5055. [[CrossRef](#)]
38. Aluha, J.; Bere, K.; Abatzoglou, N.; Gitzhofer, F. Synthesis of Nano-catalysts by Induction Suspension Plasma Technology (SPS) for Fischer-Tropsch Reaction. *Plasma Chem. Plasma Process.* **2016**, *36*, 1325–1348. [[CrossRef](#)]
39. Aluha, J.; Braidy, N.; Dalai, A.; Abatzoglou, N. Low-temperature Fischer-Tropsch synthesis using plasma-synthesised nanometric Co/C and Fe/C catalysts. *Can. J. Chem. Eng.* **2016**, *94*, 1504–1515. [[CrossRef](#)]
40. Aluha, J.; Gutierrez, S.; Gitzhofer, F.; Abatzoglou, N. Use of Plasma-Synthesized Nano-Catalysts for CO Hydrogenation in Low-Temperature Fischer-Tropsch Synthesis: Effect of Catalyst Pre-Treatment. *Nanomaterial* **2018**, *8*, 822. [[CrossRef](#)]
41. Hong, J.; Du, J.; Wang, B.; Zhang, Y.; Liu, C.; Xiong, H.; Sun, F.; Chen, S.; Li, J. Plasma-Assisted Preparation of Highly Dispersed Cobalt Catalysts for Enhanced Fischer-Tropsch Synthesis Performance. *ACS Catal.* **2018**, *8*, 6177–6185. [[CrossRef](#)]
42. Aluha, J.; Gitzhofer, F.; Abatzoglou, N. Application of Plasma Technology in Fischer-Tropsch Catalysis for the Production of Synthetic Fuels. *Recent Adv. Petrochem. Sci.* **2018**, *5*, 1–11. [[CrossRef](#)]
43. Li, D.; Rohani, V.; Fabry, F.; Ramaswamy, A.P.; Sennour, M.; Fulcheri, L. Experimental study on plasma-catalytic synthesis of hydrocarbons from syngas. *Appl. Catal. A Gen.* **2019**, *588*, 117269. [[CrossRef](#)]
44. Akay, G.; Zhang, K.; Al-Harrasi, W.S.S.; Sankaran, R.M. Catalytic Plasma Fischer-Tropsch Synthesis Using Hierarchically Connected Porous Co/SiO<sub>2</sub> Catalysts Prepared by Microwave-Induced Co-assembly. *Ind. Eng. Chem. Res.* **2020**, *59*, 12013–12027. [[CrossRef](#)]

45. Zabidi, N.A.M.; Ali, S.; Subbarao, D. Effects of Pressure on the Performance of CNTs-Supported Catalyst in a Fischer-Tropsch Reaction. *J. Mater. Sci. Eng. B* **2014**, *4*, 28–33.
46. De la Pena O'Shea, V.; Alvarez-Galvan, M.; Campos-Martin, J.; Fierro, J. Strong dependence on pressure of the performance of a Co/SiO<sub>2</sub> catalyst in Fischer-Tropsch slurry reactor synthesis. *Catal. Lett.* **2005**, *100*, 105–116. [[CrossRef](#)]
47. Ma, W.; Jacobs, G.; Ji, Y.; Bhatelia, T.; Bukur, D.B.; Khalid, S.; Davis, B.H. Fischer-Tropsch Synthesis: Influence of CO Conversion on Selectivities, H<sub>2</sub>/CO Usage Ratios, and Catalyst Stability for a Ru Promoted Co/Al<sub>2</sub>O<sub>3</sub> Catalyst Using a Slurry Phase Reactor. *Top. Catal.* **2011**, *54*, 757–767. [[CrossRef](#)]
48. Borg, Ø.; Eri, S.; Blekkan, E.A.; Storsæter, S.; Wigum, H.; Rytter, E.; Holmen, A. Fischer-Tropsch synthesis over  $\gamma$ -alumina-supported cobalt catalysts: Effect of support variables. *J. Catal.* **2007**, *248*, 89–100. [[CrossRef](#)]
49. Bukur, D.B.; Pan, Z.; Ma, W.; Jacobs, G.; Davis, B.H. Effect of CO Conversion on the Product Distribution of a Co/Al<sub>2</sub>O<sub>3</sub> Fischer-Tropsch Synthesis Catalyst Using a Fixed Bed Reactor. *Catal. Lett.* **2012**, *142*, 1382–1387. [[CrossRef](#)]
50. Botes, F.G. Influences of Water and Syngas Partial Pressure on the Kinetics of a Commercial Alumina-Supported Cobalt Fischer-Tropsch Catalyst. *Ind. Eng. Chem. Res.* **2009**, *48*, 1859–1865. [[CrossRef](#)]
51. Deprez, N.; McLachlan, D. The analysis of the electrical conductivity of graphite conductivity of graphite powders during compaction. *J. Phys. D Appl. Phys.* **1988**, *21*, 101. [[CrossRef](#)]
52. Fulcheri, L.; Rohani, V.; Fabry, F.; Traisnel, N. Experimental electrical characterization of a low-current tip-tip arc discharge in helium atmosphere at very high pressure. *Plasma Sources Sci. Technol.* **2010**, *19*, 045010. [[CrossRef](#)]
53. Benilov, M.; Marotta, A. A model of the cathode region of atmospheric pressure arcs. *J. Phys. D Appl. Phys.* **1995**, *28*, 1869–1882. [[CrossRef](#)]
54. Benilov, M.S. Understanding and modelling plasma-electrode interaction in high-pressure arc discharges: A review. *J. Phys. D Appl. Phys.* **2008**, *41*, 144001. [[CrossRef](#)]
55. Lebouvier, A.; Iwarere, S.A.; Ramjugernath, D.; Fulcheri, L. 3D magnetohydrodynamic modelling of a dc low-current plasma arc batch reactor at very high pressure in helium. *J. Phys. D Appl. Phys.* **2013**, *46*, 145203. [[CrossRef](#)]
56. Cheng, D.-G. Plasma Decomposition and Reduction in Supported Metal Catalyst Preparation. *Catal. Surv. Asia* **2008**, *12*, 145–151. [[CrossRef](#)]
57. Bakhtiari, M.; Khorasheh, F.; Zamanian, A.; Nakhaeipour, A.; Irani, M. Preparation, Evaluation and Characterization of Monolithic Catalysts for Fischer-Tropsch Synthesis. *Pet. Coal* **2008**, *50*, 56–61.
58. Khodakov, A.Y.; Chu, W.; Fongarland, P. Advances in the Development of Novel Cobalt Fischer-Tropsch Catalysts for Synthesis of Long-Chain Hydrocarbons and Clean Fuels. *Chem. Rev.* **2007**, *107*, 1692–1744. [[CrossRef](#)]
59. Kim, H.H. Nonthermal Plasma Processing for Air-Pollution Control: A Historical Review, Current Issues, and Future Prospects. *Plasma Process. Polym.* **2004**, *1*, 91–110. [[CrossRef](#)]
60. Chang, M.B.; Lee, H.M. Abatement of perfluorocarbons with combined plasma catalysis in atmospheric-pressure environment. *Catal. Today* **2004**, *89*, 109–115. [[CrossRef](#)]
61. Yu, S.J.; Chang, M.B. Oxidative Conversion of PFC via Plasma Processing with Dielectric Barrier Discharges. *Plasma Chem. Plasma Process.* **2001**, *21*, 311–327. [[CrossRef](#)]
62. Holzer, F.; Roland, U.; Kopinke, F.-D. Combination of non-thermal plasma and heterogeneous catalysis for oxidation of volatile organic compounds: Part 1. Accessibility of the intra-particle volume. *Appl. Catal. B Environ.* **2002**, *38*, 163–181. [[CrossRef](#)]
63. Chen, X.; Rozak, J.; Lin, J.-C.; Suib, S.L.; Hayashi, Y.; Matsumoto, H. Oxidative decomposition of chlorinated hydrocarbons by glow discharge in PACT (plasma and catalyst integrated technologies) reactors. *Appl. Catal. A Gen.* **2001**, *219*, 25–31. [[CrossRef](#)]
64. Rueangjitt, N.; Sreethawong, T.; Chavadej, S.; Sekiguchi, H. Non-Oxidative Reforming of Methane in a Mini-Gliding Arc Discharge Reactor: Effects of Feed Methane Concentration, Feed Flow Rate, Electrode Gap Distance, Residence Time, and Catalyst Distance. *Plasma Chem. Plasma Process.* **2011**, *31*, 517–534. [[CrossRef](#)]
65. Rueangjitt, N.; Sreethawong, T.; Chavadej, S.; Sekiguchi, H. Plasma-catalytic reforming of methane in AC microsized gliding arc discharge: Effects of input power, reactor thickness, and catalyst existence. *Chem. Eng. J.* **2009**, *155*, 874–880. [[CrossRef](#)]
66. Hilmen, A.-M.; Bergene, E.; Lindvåg, O.; Schanke, D.; Eri, S.; Holmen, A. Fischer-Tropsch synthesis on monolithic catalysts of different materials. *Catal. Today* **2001**, *69*, 227–232. [[CrossRef](#)]
67. Hilmen, A.-M.; Bergene, E.; Lindvåg, O.; Schanke, D.; Eri, S.; Holmen, A. Fischer-Tropsch synthesis using monolithic catalysts. *Stud. Surf. Sci. Catal.* **2000**, *130*, 1163–1168. [[CrossRef](#)]
68. de Deugd, R.M.; Chougule, R.B.; Kreutzer, M.T.; Meeuse, F.M.; Grievink, J.; Kapteijn, F.; Moulijn, J.A. Is a monolithic loop reactor a viable option for Fischer-Tropsch synthesis? *Chem. Eng. Sci.* **2003**, *58*, 583–591. [[CrossRef](#)]
69. De Deugd, R.M.; Kapteijn, F.; Moulijn, J.A. Using monolithic catalysts for highly selective Fischer-Tropsch synthesis. *Catal. Today* **2003**, *79*, 495–501. [[CrossRef](#)]
70. Kapteijn, F.; de Deugd, R.M.; Moulijn, J.A. Fischer-Tropsch synthesis using monolithic catalysts. *Catal. Today* **2005**, *105*, 350–356. [[CrossRef](#)]
71. Guettel, R.; Knochen, J.; Kunz, U.; Kassing, M.; Turek, T. Preparation and Catalytic Evaluation of Cobalt-Based Monolithic and Powder Catalysts for Fischer-Tropsch Synthesis. *Ind. Eng. Chem. Res.* **2008**, *47*, 6589–6597. [[CrossRef](#)]
72. Liu, W.; Hu, J.; Wang, Y. Fischer-Tropsch synthesis on ceramic monolith-structured catalysts. *Catal. Today* **2009**, *140*, 142–148. [[CrossRef](#)]

73. Avila, P.; Montes, M.; Miro, E.E. Monolithic reactors for environmental applications: A review on preparation technologies. *Chem. Eng. J.* **2005**, *109*, 11–36. [[CrossRef](#)]
74. Panneerselvam, M.; Rao, K. Novel Microwave Method for the Synthesis and Sintering of Mullite from Kaolinite. *Chem. Mater.* **2003**, *15*, 2247–2252. [[CrossRef](#)]
75. Chaudhuri, S.; Patra, S.; Chakraborty, A. Electrical resistivity of transition metal ion doped Mullite. *J. Eur. Ceram. Soc.* **1999**, *19*, 2941–2950. [[CrossRef](#)]
76. Schneider, H.; Schreuer, J.; Hildmann, B. Structure and properties of mullite—A review. *J. Eur. Ceram. Soc.* **2008**, *28*, 329–344. [[CrossRef](#)]
77. Villegas, L.; Masset, F.; Guilhaume, N. Wet impregnation of alumina-washcoated monoliths: Effect of the drying procedure on Ni distribution and on autothermal reforming activity. *Appl. Catal. A Gen.* **2007**, *320*, 43–55. [[CrossRef](#)]
78. Holmen, A.; Venvik, H.J.; Myrstad, R.; Zhu, J.; Chen, D. Monolithic, microchannel and carbon nanofibers/carbon felt reactors for syngas conversion by Fischer-Tropsch synthesis. *Catal. Today* **2013**, *216*, 150–157. [[CrossRef](#)]